Practical Aspects and Advanced Applications of XEDS

17

Chapter Preview

The details and applications of X-ray analysis in TEM were described comprehensively in Chaps. 32–36 of W&C. These chapters cover all essential topics you should know prior to your own applications of X-ray analysis; from the fundamentals of spectrometers, qualitative elemental analysis, and quantitative composition determination through advanced spatial resolution and analytical sensitivity of XEDS. The main objective of this chapter is to complement W&C by introducing more advanced XEDS approaches in the TEM while not increasing the level of difficulty. This chapter consists of four sections

– Practical characterization of XEDS detectors in TEM.
– Simulation of X-ray spectra for thin-film analysis.
– Details of quantitative X-ray analysis of thin-films by the ζ-factor method.
– Contemporary topics including recent advances in X-ray analysis.

Each section is independent of the others, but closely related to corresponding chapters in W&C. In addition to Chaps. 32-36 of W&C, you can also read Lyman et al (1990), Williams and Goldstein (1991) and Zemyan and Williams (1995) on fundamentals of X-ray analysis in TEM.

17.1 Performance Parameters of XEDS Detectors

As we suggested in Chaps. 32 and 33 of W&C, you need to know about your XEDS detector in terms of its fundamental performance parameters before utilizing it for any practical analysis. You should measure some detector parameters at least once when your system is installed or significantly upgraded. Other parameters also need to be measured time to time to monitor your system performance in a consistent manner. Fortunately, you can measure most of the XEDS characteristics using Egerton's NiOx test specimen (Egerton, Cheng, 1994); this is why W&C strongly recommends that you purchase the NiOx film or similar NiO films – the x is nicely ambiguous!

> **The NiOx Test Specimen**
>
> It consists of ~50-nm-thick NiO film on ~20-nm-thick amorphous carbon support on a 200 mesh Mo grid. Be careful if you make your own!   ◄

You can use this test specimen for calibrations of the camera length, aperture angles, EELS analysis, etc. Besides those calibrations, the following parameters can be determined for XEDS-based applications from a single XEDS spectrum of the NiOx thin film

- Detector energy resolution: described in Sect. 32.8 of W&C.
- Peak-to-background ratio in general and the Fiori definitions: mentioned in Sect. 33.4A of W&C.
- Inverse hole-count (a.k.a film count): explained in Sect. 33.3A of W&C.
- Mo K/L ratio: described in Sect. 33.3A of W&C.
- Detector collection angle: described in Sect. 32.10A of W&C.
- Detector efficiency: defined in Sect. 33.4B of W&C.

You can find detailed descriptions about these various determinations in Egerton's original papers. In addition, you can also monitor some of the detector parameters (such as thicknesses of ice and carbon in front of the active area) if you gather several spectra from the NiOx film over different time periods. The detection of X-rays from light elements (which produce low-energy soft X-rays) is significantly influenced by the thicknesses of these various layers. You can measure quantitatively the growth of ice and carbon layers, which directly degrade detection of these soft X-rays. In this section, we will show you how to measure these parameters in practice and will introduce software that allows you to carry out these measurements easily.

17.1.1 Detector, Fundamental Parameters

Energy Calibration: The X-ray energy range and dispersion must be calibrated before performing any X-ray analysis or even before applying any measurement of the following fundamental system parameters in AEM. By using the NiOx test specimen, you can easily calibrate the energy dispersive range with the Ni Kα peak at 7.48 keV, in combination with either the O Kα peak (0.52 keV) or the Ni Lα peak (0.85 keV). If you need to calibrate the energy range >10 keV then you can use the Mo Kα peak at 17.42 keV. Although any characteristic X-ray signal from the grid bar is always undesirable (since it proves there are spurious X-ray signals in your spectrum), the high-energy X-ray peak is actually useful for this calibration.

Detector Energy, Resolution: We define the energy resolution of an XEDS detector as the full-width at half-maximum (FWHM) value at the Mn Kα peak position (5.9 keV). You can derive this value from the FWHM value of the Ni Kα peak in an XEDS spectrum from the NiOx film as described by Bennett and Egerton (1995)

$$R_{\mathrm{FWHM}}(\mathrm{Mn K}\alpha) = 0.926\, R_{\mathrm{FWHM}}(\mathrm{Ni K}\alpha) \tag{17.1}$$

The FWHM value of the Ni Kα peak can be best determined by fitting to a Gaussian, as shown in Fig. 17.1a. You can see that the Gaussian fit curve deviates slightly from the Ni Kα peak on the low-energy side. This deviation from the Gaussian is mainly caused by incomplete charge collection, which can be evaluated if you measure the ratio of the full-width at tenth-maximum (FWTM) to the FWHM values of the peak (see Sect. 32.9A in W&C).

> **Take Time**
>
> The longer the process-time setting, the better the detector energy resolution. A higher number on the x-axis of the plot gives a lower energy range.   ◄

The detector energy resolution depends on how you set the process time (or time constant). If you choose a shorter process time, the energy resolution is degraded despite having higher count rates. Figure 17.1b shows the detector energy resolution measured from three different AEMs with a Si(Li) detector operated at 100, 200 and 300 kV, plotted against the process-time setting.

Peak-to-Background Ratio: We can use the peak-to-background (P/B) ratio as a measure to describe how well the XEDS-AEM system is configured. Typically a higher P/B value indicates a better-configured system. As described in Sect. 33.4A of W&C, there are a number of definitions for P/B. The most common definition is to use the full peak intensity and the background intensity with the same energy window as the peak.

The above definition of P/B may depend on the energy resolution of the spectrometer system since the energy window size for the background varies with the energy resolution. To compare the P/B values taken from different instruments (or
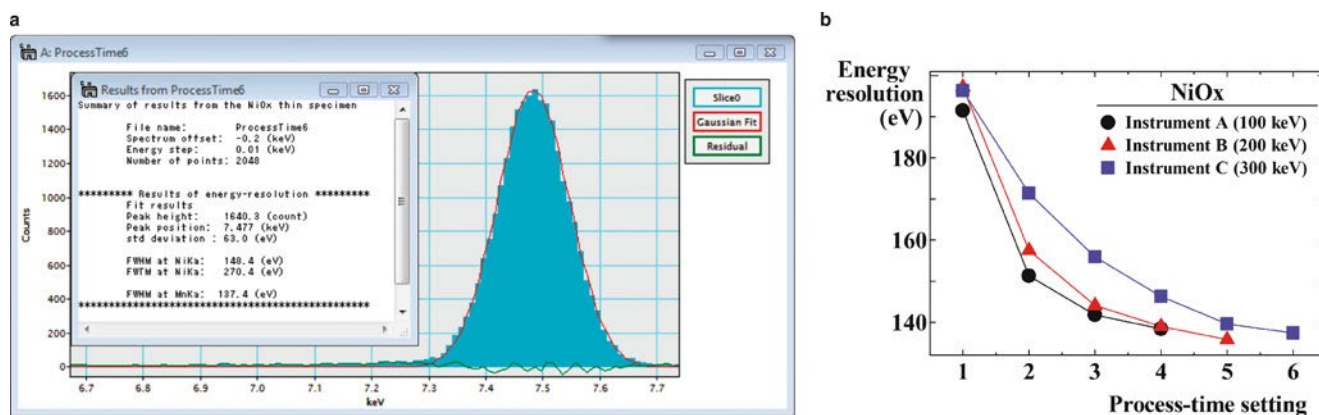
Fig. 17.1 a Example of energy resolution determination using the Ni Kα peak from the NiOx test specimen. For the determination, the NiOx plug-in in Gatan DigitalMicrograph was used. **b** The determined energy resolution of XEDS systems of three different instruments (100, 200, and 300 kV), plotted against the process time setting

even at different process time setting) fairly, you should use the Fiori definition for *P/B* (Fiori et al. 1982), in which the average background intensity at a single channel (e.g., 10 eV) is used rather than the full background intensity. The typical energy windows of characteristic X-ray lines for the NiOx are summarized in Table 17.1. The background intensities are ideally determined by averaging two intensities at lower and higher energy regions of the peak. According to Bennett and Egerton, this value for the Ni Kα from the NiOx test specimen can be as high as 3,000 in modern commercial 200-kV-AEMs. If a pure-element film such as a Cr film is used, your measured *P/B* value should be higher than that from the NiOx film because the Cr Kα intensity corresponds to 100 wt% in the pure Cr film, whereas the Ni Kα intensity represents 78.6 wt% in the NiOx film (50 : 50 in atomic ratio).

Table 17.1 Typical energy windows of characteristic X-ray lines for the NiOx (Lyman et al. 1994)

X-ray line	Energy window range (keV)		
	Peak (P)	Background 1 (B₁)	Background 2 (B₂)
O Kα	0.38–0.64	1.10–1.36	
Ni Lα	0.68–1.00	1.10–1.42	
Ni Kα	7.16–7.76	6.50–7.10	8.60–9.20
Mo Lα	2.16–2.50	1.10–1.44	3.00–3.34
Mo Kα	17.04–17.80	16.10–16.86	18.14–18.90

Inverse Hole Count (Film Count): The inverse hole count (IHC) is another useful measure we can use to evaluate the presence of stray electrons and X-rays in an AEM column. We define IHC as the intensity ratio of a major X-ray line in the specimen (which should be detected) to an X-ray line from a grid material (which should not be detected in an ideal column). In the NiOx test specimen, IHC is given as the ratio of the intensities of the Ni Kα to the Mo Kα peaks above background. In modern commercial AEMs, this value is usually in range from 3–7.

Using the *P/B* and IHC values determined from a single spectrum in the NiOx test specimen, you can evaluate the performance of your specific XEDS-AEM. Figure 17.2 shows a plot of *P/B* (the Fiori definition) against the IHC, measured in three different instruments operated at 100, 200 and 300 kV (these are actually the same instruments in Fig. 17.1b). The error bars indicate a 99 % confidence limit (3σ). As we mentioned above, higher values both of *P/B* and IHC are preferable. Therefore, instruments at the top right-hand corner should give superior X-ray analyses.

Mo K/L Ratio: You can use the ratio of the Mo Kα to the Mo Lα intensities to evaluate stray irradiation in your instrument as was

described in Sect. 33.3.A of W&C. Stray X-rays would produce a high Mo K/L ratio since high-energy bremsstrahlung X-rays preferentially fluoresce the high-energy Mo Kα line. In contrast, stray electrons would excite the Mo Lα rather than the Mo Kα. Generally, the Mo K/L ratio decreases with an increase of the probe-forming aperture size and increases with an increase in the incident electron energy. Thus, using the Mo K/L value, you can diagnose stray irradiations of the illumination system in your instrument.

Detector Collection Angle: As mentioned in Sect. 32.10A of W&C, the collection angle for X-ray detection (Ω) is the most important parameter in all of X-ray analysis. We generally want to detect more X-rays, so a larger Ω value is always preferable. In fact, you may use the latest silicon drift detectors (SDDs) with significantly improved solid angle as described later in Sect. 17.4. You can measure the Ω value nominally from the geometric configuration of your AEM-XEDS interface, using Eq. 32.4 in W&C. However, such a practical measurement of Ω is not very straightforward. The Ω measurement requires that you take a reference spectrum from a known standard in a specific instrument with calibrated Ω in order to compare X-ray intensities.

Chapter 17
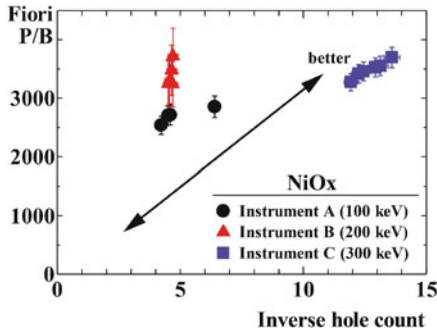
Fig. 17.2 Determined P/B (Fiori definition) plotted against the IHC, measured from three different instruments operated at 100, 200, and 300 kV

Fig. 17.3 Comparison of X-ray spectra obtained from the same NiOx test specimen in the same instrument at different periods of time

Table 17.2 A prefactor C_1 for Ω determination at a given an incident beam energy E_0 (Bennett and Egerton, 1995).

E_0 (kV)	80	100	120	200	300	400
C_1	2.6	2.9	3.2	4.0	4.8	5.3

Fortunately, we can use an empirical formula for the Ω determination based on a single NiOx spectrum

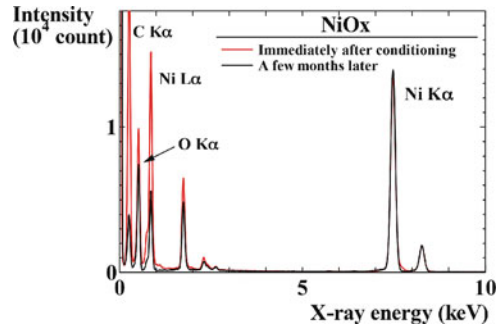$$\Omega = C_1 \cos\theta \, I_{\mathrm{NiK}}/(t\,\tau\,I_\mathrm{p}) \tag{17.2}$$

where C_1 is a factor depending on the incident beam energy (summarized in Table 17.2 or you can calibrate it beforehand), I_{NiK} is the Ni Kα intensity above the background, t is the film thickness, τ is the acquisition time and I_p is the probe current, respectively. In addition, θ is the total tilt angle including tilt angles in both x and y directions (θ_x and θ_y, respectively) and simply given as:

$$\theta = \tan^{-1}\left(\sqrt{\tan^2\theta_x + \tan^2\theta_y}\right) \tag{17.3}$$

Relative Detector Efficiency: Once you have measured a more accurate Ω value through Eq. 17.2, the relative detector efficiency can be determined. We define this relative detector efficiency in terms of how many X-ray counts per second are collected from a standard specimen (such as the pure Cr film and the NiOx specimen) in the measured collection angle (sr) with the incident probe current (nA). The relative detector efficiency can then be given as:

$$(\textit{relative detector efficiency}) = I_{\mathrm{NiK}}/(\tau I_p \Omega)(\mathrm{cps/nA/sr}) \tag{17.4}$$

You should measure all the parameters described above at least once, ideally when your system is installed. If you don't know these parameters, it is not too late to determine them now. The determination is straightforward since only *a single spectrum* needs to be acquired from your NiOx test specimen.

## 17.1.2 Monitoring Detector Contamination

The detection performance of your XEDS detector may change considerably with time, especially in its ability to detect low-energy, soft X-rays. For example, Fig. 17.3 compares two X-ray spectra acquired from the NiOx film in the same instrument with a windowless XEDS detector at different time periods (one was recorded just after detector conditioning and other was a few months later). As you can see, although there is no noticeable difference in the Ni Kα line, the intensity level is significantly reduced in the lower-energy O Kα and Ni Lα peaks. This difference in the X-ray detection efficiency at lower energy regions may lead to serious problems, especially if you are carrying out quantitative analysis using lower-energy soft X-rays.

> **Residual Gases**
>
> In a typical microscope column, the major residual gases are water vapor and hydrocarbons. ◄

Such degradation of soft X-ray detection can be caused by contamination (mainly in front of the detector window) and the degradation rate is strongly related to the vacuum conditions of your instrument. The active area of your detector (an XEDS detector should be cooled by liquid N_2 or by a Peltier device) easily condenses water vapor into an ice layer, and hydrocarbons may also be condensed as a carbonaceous layer.

Figure 17.4 shows the absorption ratio of the O Kα, Ni Lα and Ni Kα lines, plotted against thickness of the ice (a) and carbon (b) layers. The ice layer build-up influences the Ni Lα line most severely. When the ice layer reaches $\sim 1\,\mu$m, 50 % of the Ni Lα intensity is absorbed in the ice layer. For the O Kα, the ice build-up is less sensitive. Over 5 μm of ice layer absorbs ~ 50 % of O Kα intensity. In contrast, the carbon layer significantly influences both the O Kα and Ni Lα lines, as shown in Fig. 17.4b.
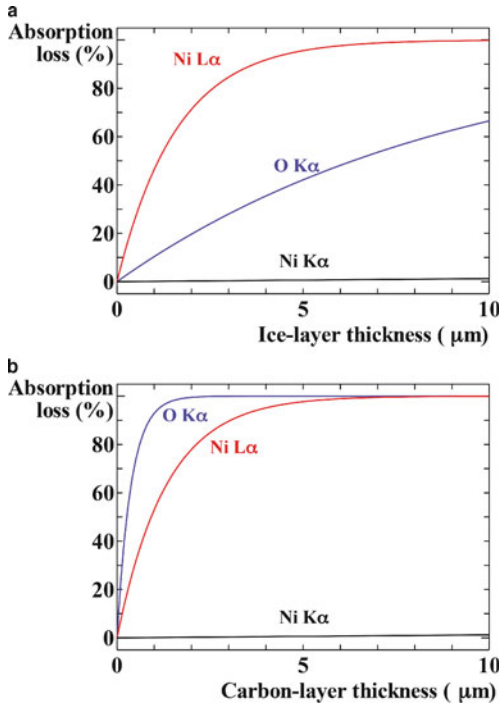
Fig. 17.4 Calculated absorption ratios of the O Kα, Ni Lα and Ni Kα lines, plotted against the ice thickness (**a**) and the carbon thickness (**b**) in front of the detector active area

With a 1 μm carbon layer, 90% of the O Kα and 50% of the Ni Lα X-rays are absorbed. Conversely, absorption of the Ni Kα X-rays is negligible both in the ice and the carbon (up to 10 μm). In addition to the reduction of soft X-ray detection, accumulation of the ice and carbon layers may also cause (1) a decrease in the background intensity even at higher energies (which results in an increase in your P/B ratio) and (2) a decrease in dead time during X-ray acquisition. Therefore, it is essential that you monitor the accumulation of ice and carbon layers on your detector.

X-ray absorption due to the ice and carbon layers can be modeled as (Hovington et al. 1993)

$$A = \exp\left[-(\mu/\rho)_O^X \rho_{ice} t_{ice} - (\mu/\rho)_C^X \rho_C t_C\right] \tag{17.5}$$

Where $(\mu/\rho)_O^X$ and $(\mu/\rho)_C^X$ are the mass absorption coefficients (MACs) of X-ray X in oxygen and carbon, ρ_{ice} and ρ_C are the densities of ice (0.917 Mg/m³) and carbon (2.267 Mg/m³), and t_{ice} and t_C are the thicknesses of ice and carbon layers. You should note that the MAC value for oxygen is used instead of that in ice in the above equation because the MAC value for hydrogen is very low for all X-rays. In particular, for the NiOx test specimen, the following equations are relevant:

$$(I_{OK}/I_{NiK}) \propto \exp\left[\chi_O^{OK} t_{ice} - \chi_C^{OK} t_C\right]$$
$$(I_{NiL}/I_{NiK}) \propto \exp\left[\chi_O^{NiL} t_{ice} - \chi_C^{NiL} t_C\right] \tag{17.6}$$

with

$$\chi_O^{OK} = \{(\mu/\rho)_O^{OK} - (\mu/\rho)_O^{NiK}\}\rho_{ice}$$
$$\chi_C^{OK} = \{(\mu/\rho)_C^{OK} - (\mu/\rho)_C^{NiK}\}\rho_C$$
$$\chi_O^{NiL} = \{(\mu/\rho)_O^{NiL} - (\mu/\rho)_O^{NiK}\}\rho_{ice}$$
$$\chi_C^{NiL} = \{(\mu/\rho)_C^{NiL} - (\mu/\rho)_C^{NiK}\}\rho_C \tag{17.7}$$

If you take ratios of the above intensity ratios (I_{OK}/I_{NiK} and I_{NiL}/I_{NiK}) between two independent measurements (subscripts 1 and 2) you can derive the following equations:

$$R_{OK} = \frac{(I_{OK}/I_{NiK})_1}{(I_{OK}/I_{NiK})_2} = \exp\left[-\chi_O^{OK}\Delta t_{ice} - \chi_C^{OK}\Delta_C\right]$$
$$R_{NiL} = \frac{(I_{NiL}/I_{NiK})_1}{(I_{NiL}/I_{NiK})_2} = \exp\left[-\chi_O^{NiL}\Delta t_{ice} - \chi_C^{NiL}\Delta_C\right] \tag{17.8}$$

where Δt_{ice} and Δt_C are thickness differences in ice and carbon layers between measurement 1 and 2, respectively, i.e., the relative layer growth of ice and carbon between your two measurements. Then, Δt_{ice} and Δt_C can be derived as:

$$\Delta t_{ice} = \frac{\chi_C^{NiL}\ln(R_{OK}) - \chi_C^{OK}\ln(R_{NiL})}{\chi_C^{OK}\chi_O^{NiL} - \chi_C^{NiL}\chi_O^{OK}}$$
$$\Delta t_C = \frac{\chi_C^{OK}\ln(R_{NiL}) - \chi_C^{NiL}\ln(R_{OK})}{\chi_C^{OK}\chi_O^{NiL} - \chi_C^{NiL}\chi_O^{OK}} \tag{17.9}$$

In the above equation, the only parameters you need are the densities of ice and carbon, and the MACs, which you can find summarized in Table 17.3. Using these parameters, Eq. 17.9 can be simplified thus:

$$\Delta t_{ice} = 481.4\ln\left[\frac{(I_{OK}/I_{NiK})_1}{(I_{OK}/I_{NiK})_2}\right] - 1689.8\ln\left[\frac{(I_{NiL}/I_{NiK})_1}{(I_{NiL}/I_{NiK})_2}\right]$$
$$\Delta t_C = 69.0\ln\left[\frac{(I_{NiL}/I_{NiK})_1}{(I_{NiLw}/I_{NiK})_2}\right] - 397.2\ln\left[\frac{(I_{OK}/I_{NiK})_1}{(I_{OK}/I_{NiK})_2}\right] \quad (nm)$$

$$\tag{17.10}$$

In the derivation of Eq. 17.10, we used the MAC values reported by Heinrich 1987. If you want to determine the contamination layer thicknesses, you have to take two spectra in almost identical conditions, i.e., with the same specimen tilt, time constant, etc. However, by taking the double ratio, you can cancel out any differences in the acquisition time and the probe current.

17.1.3 Software to Determine Detector Parameters

You can measure many detector parameters including the decay of detector performance by acquiring a single spectrum

Table 17.3 Summary of parameters for determination of contamination layer growth at an XEDS window. The MAC values are calculated from Heinrich's formula (Heinrich 1987)

For ice	For carbon
$\rho_{ice} = 0.917\,Mg/m^3$	$\rho_C = 2.267\,Mg/m^3$
$(\mu/\rho)_O^{OK} = 119.3\,m^2/kg$	$(\mu/\rho)_C^{OK} = 1{,}168.6\,m^2/kg$
$(\mu/\rho)_O^{NiL} = 680.3\,m^2/kg$	$(\mu/\rho)_C^{NiL} = 333.3\,m^2/kg$
$(\mu/\rho)_O^{NiK} = 1.395\,m^2/kg$	$(\mu/\rho)_C^{NiK} = 0.545\,m^2/kg$

or a set of spectra from the NiOx test specimen. To perform these measurements routinely and consistently, use the plug-in for Gatan DigitalMicrograph. To run any functionalities in this plug-in package, you have to have Gatan DigitalMicrograph (see Chap. 6). Next, we'll introduce two additional plug-ins, in which all the evaluation procedures of detector performance described above are implemented.

NiOx: this plug-in determines all the fundamental detector parameters described in Sect. 17.1.1 above. Figure 17.5a shows the dialog of the NiOx plug-in. All you need to do is to i) open a spectrum from the NiOx test specimen, ii) select the detector parameters you want to determine by clicking the check boxes, and (iii) click the 'Calculate' button. If you select the 'Solid angle and Relative detector efficiency', an additional sub-dialog appears (Fig. 17.5b) so you can input several instrumental and experimental parameters. An example of the output is shown in Fig. 17.5c.

NiOxIceC: this plug-in determines the accumulated ice and carbon thicknesses from two spectra measured in different time period from your NiOx test specimen. As we already mentioned above, you must acquire these spectra in the same instrument under almost identical experimental conditions. Figure 17.6 shows the dialog of the plug-in (A) and an example of the output (B) from the two spectra shown in Fig. 17.3. In this particular case, the accumulated ice and carbon layers are $1.67 \pm 0.04\,\mu m$ and $53.1 \pm 8.5\,nm$ with 99 % confidence limits (3σ), respectively.

In addition to these plug-ins, this package also contains a function to import a spectrum in the EMSA/MAS file format (EMSA file import). The EMSA/MAS file format is the one most commonly used in the electron microscopy community and most XEDS manufactures support this format in their systems. You should check the system manual or consult the manufacturer to find out how to save a spectrum in the EMSA format. As long as your spectrum is saved in the EMSA format, you can convert it to DigitalMicrograph and your detector parameters can be determined via the above plug-ins. You can find a standardized description of the EMSA format through the International Organization for Standardization.

17.2 X-ray Spectrum Simulation – a Tutorial and Applications of DTSA

Planning your experiments is one of the most important tasks for all microscopists because preparation for TEM experiments, including specimen preparation and actual microscopy sessions, requires significant amounts of time and money – the cost of running and maintaining a TEM – it's not free! In order to plan (or ideally to optimize) your experiments, it would be very efficient to predict i) the feasibility of each experiment, ii) difficulties of measurements, and iii) the fundamental limits of planned analyses. Theoretical simulation is one of the best approaches to confirm your experimental limits before you conduct actual experiments if, of course, appropriate simulation tools are available.

Fortunately, for XEDS, several tools are available to simulate an X-ray spectrum: some are based on a first principles approach such as DTSA (Fiori et al. 1992) while others are combined with Monte Carlo techniques, e.g., the electron flight simulator (Brundle et al. 1996). (See References for Software for both.) In the current version of DTSA-II (Ritchie 2008), however, the function for spectrum simulation is only available for bulk samples. While writing, we are still waiting for a thin-film version of the spectrum generation. Therefore, in this section, we will explain X-ray spectrum simulation using DTSA instead. Perhaps the thin-film version of X-ray spectrum simulation will be implemented in either DTSA-II or other modern software packages by the time you are reading this chapter.

> **DTSA**
>
> The most recent version of DTSA is DTSA-II; it includes both a first principles approach and Monte Carlo techniques. Use it to generate X-ray spectra before you go to TEM. ◄

In order to simulate an X-ray spectrum properly, you need to understand several fundamental parameters related to X-ray generation and detection. After we introduce DTSA in this section, we'll illustrate the fundamental parameters for X-ray analysis by a brief tutorial for the X-ray spectrum simulation. Then, we'll explain further details of X-ray generation and detection by simulating several different stages of X-ray spectra, (which are never actually seen in practice) for example what an X-ray spectrum looks like before it is emitted from your specimen and before it is processed by the XEDS detector electronics, etc. We can only demonstrate this feature by a first principles simulation, which is very useful to help you understand the physics behind X-ray generation and detection.

Once you understand the appropriate procedures for X-ray spectrum simulation using DTSA, you will be ready to apply it to
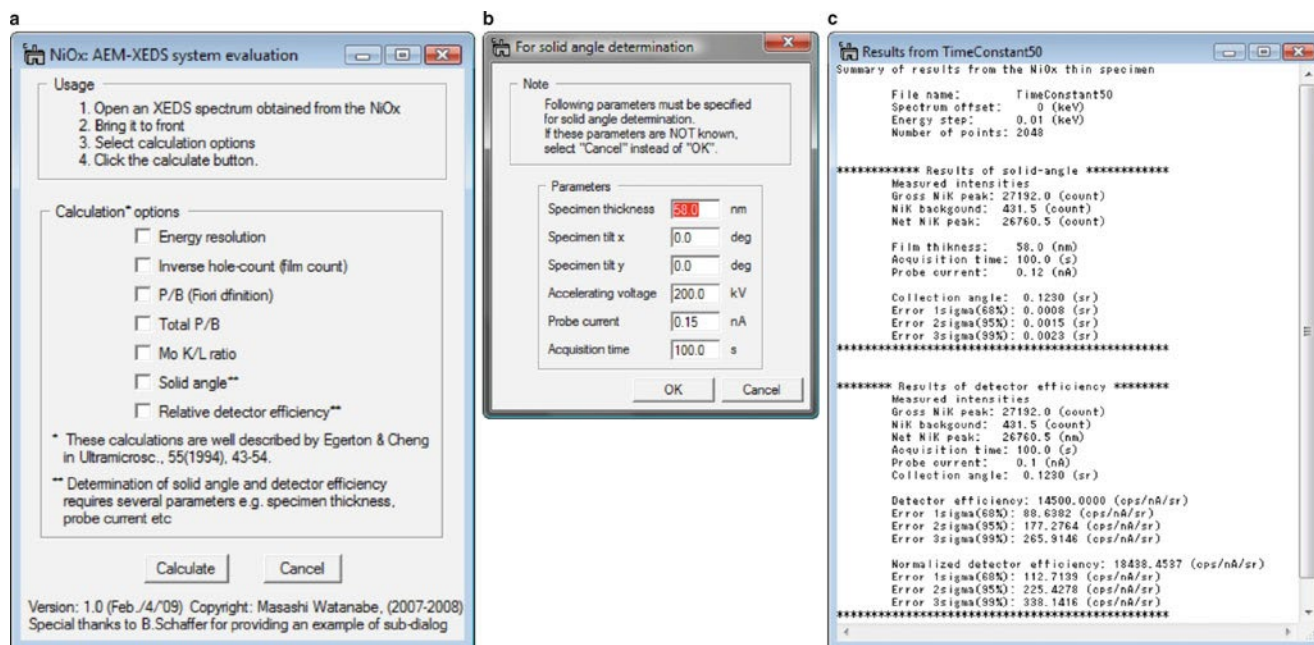
Fig. 17.5 a Main dialog of the NiOx plug-in package. **b** Sub-dialog for determination of the collection angle and the relative detector efficiency, and **c** An example of the output for the determination of the collection angle and the relative detector efficiency in a 200 kV instrument
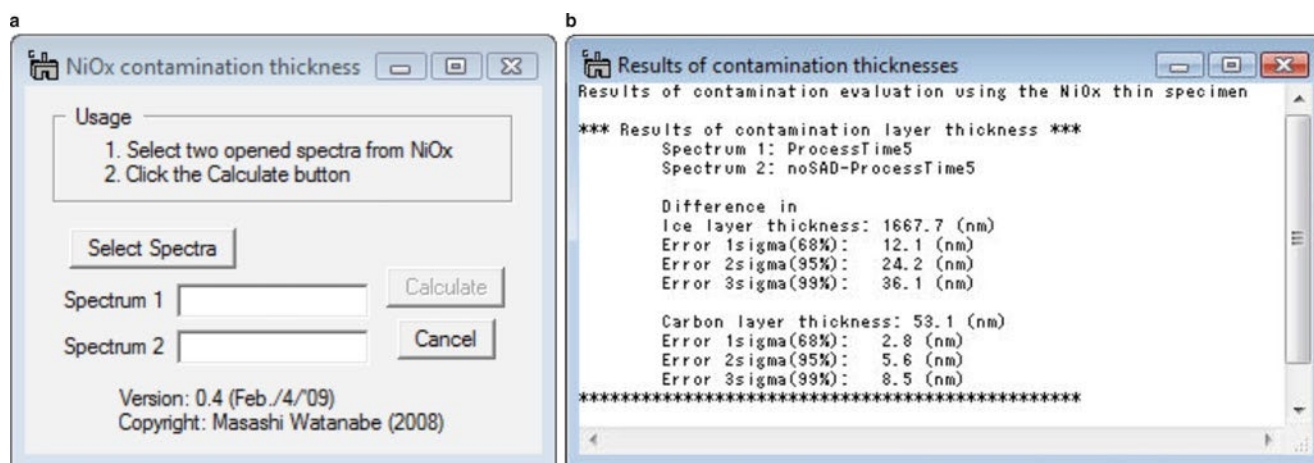

Fig. 17.6 a Main dialog of the NiOxIceC plug-in package. **b** An example of the output for determination of the accumulated layer thicknesses of ice and carbon, measured in a 300 kV UHV instrument with a windowless XEDS detector

predict your experimental spectra. Finally, we'll show you four practical applications of the X-ray spectrum simulation at the end of this section. These four are

- Confirmation of peak overlap (related to Sect. 34.3 of W&C),
- Evaluation of X-ray absorption in a thin specimen (related to Sect. 35.6 of W&C),
- Demonstration of AEM-XEDS interfaces (related to Sect. 33.4A of W&C),
- Estimation of the detectability limits (see Sect. 34.4 and 36.4 of W&C).

17.2.1 What Is DTSA?

The function of an electron-excited X-ray spectrum generator is one of the main features of DTSA, which was implemented as a 'dry lab' by Fiori to predict experimental limits. This generator is available both for bulk samples and for thin films. Besides this powerful feature, DTSA provides several useful functions for X-ray analysis such as peak deconvolution, background subtraction, quantitative matrix corrections for bulk samples and Cliff–Lorimer quantification for thin speci-
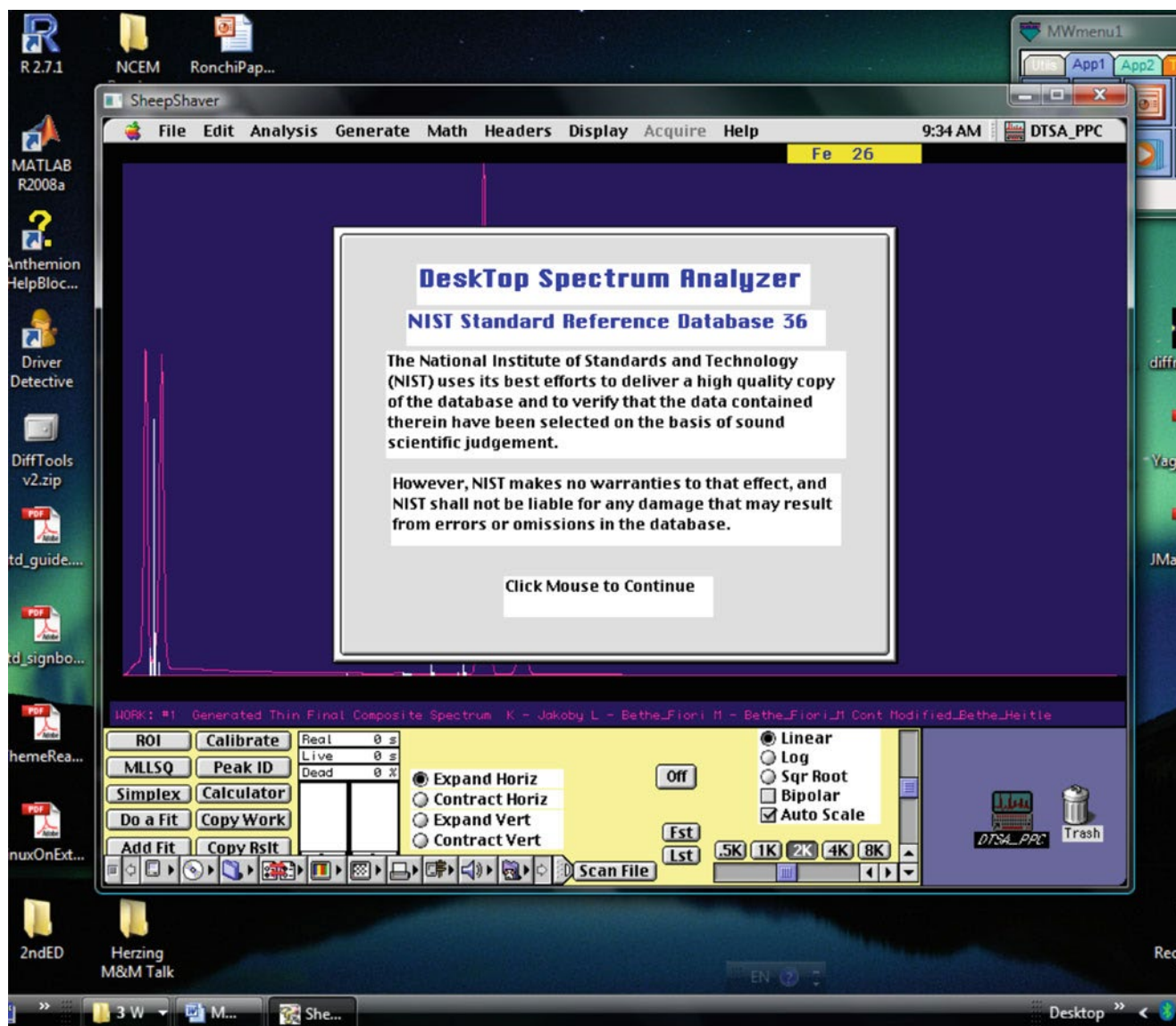
Chapter 17

Fig. 17.7 Screen shot of DTSA running via SheepShaver under a Windows platform

mens, along with a comprehensive database related to X-ray analysis.

Fiori developed the original version of DTSA using the Pascal program language for an Apple Macintosh II and the last versions (2.5 or 3.0.1) run in a Power Macintosh under classic OS 8 and 9. DTSA does run under the so-called classic mode in OS X if the CPU is either G4 or G5. However, the DTSA runs neither in a newer Mac with an Intel CPU nor in any Windows/ Linux PC. So, we keep an iMac (generation 2000) just to run DTSA! While many of you will not have access to such museum pieces, fortunately, DTSA-II (the successor to DTSA) has been developed as a JAVA-based, platform-free, software by Nicho-

las Ritchie at NIST, and hence can run in Windows, Mac OS X and Linux. Therefore, in the near future, all the descriptions in this section may be replaced with those adjusted for DTSA-II, once DTSA-II provides the spectrum generation function for thin films!

We should mention that you can run the PowerMac version (2.5) of DTSA either in Windows (as shown in Fig. 17.7) or in Mac OS X, or even in Linux, via a PowerMac emulator called 'Sheep-Shaver' (see References to find this software package). So, while it is a temporary solution for now, it should also work for Mac OS X and Linux systems.

17.2.2 A Brief Tutorial of X-ray Spectrum Simulation for a Thin Specimen Using DTSA

Once you successfully launch DTSA, select 'Generate > Thin Target Spectrum' from the pull-down menu to simulate an X-ray spectrum for a thin specimen. Then, the main dialog for thin-specimen spectrum generation appears as shown in Fig. 17.8. In this main dialog and subsequent dialogs, you can fill in or select the parameters required for simulation. Note that you can also simulate an X-ray spectrum for a bulk sample when 'Bulk Target Spectrum' is selected. The difference between the bulk and thin targets is minimal with respect to parameter set-up for spectrum simulation.

Detector Parameters: If you click the 'Detector Parameters' button in the main dialog, you'll see that a dialog for detector parameters appears (Fig. 17.9a). In this dialog, you can (A) select/input several detector configuration parameters and (B) define the detector-window parameters. Select your detector type (either Si or Ge) and input the energy resolution that you should have determined using the NiOx specimen and any other parameters associated with your detector and window configurations. If you are not sure about your specific detector configuration, consult the lab manager or the manufacturer, or take values from Table 32.1 in W&C. You can also load typical values by clicking the 'Load Typical Values' button (remember however, these typical values could be very different from those for your particular instrument). It should be mentioned that many XEDS detectors attached to modern AEMs are Si(Li) detectors or SDDs with an atmospheric thin-window (ATW), which has a Moxtek polymer layer of ~0.3 μm and an Al contact layer of ~0.04 μm, as shown in Fig. 17.9a.

> **Typical Detector Configurations**
>
> In modern instruments the take-off angle is 20–25° and the specimen-detector distance is ~15 mm or less. ◄

After setting up the above parameters, click the 'Detector-Specimen Geometry Dialog' button (C). Another sub-dialog appears in which you can input the geometry configuration between the XEDS detector and instrument, as shown in Fig. 17.9b. There are two most important parameters you have to input in this dialog, namely the 'Detector Elevation Angle' corresponding to the X-ray take-off angle and the 'Specimen-Detector Distance' that controls the X-ray collection angle (see Sect. 32.10A of W&C). Again, you should consult the manufacturer if you are not aware of these parameters. Alternatively, you can reverse-calculate the specimen-detector distance from the detector collection angle using Eq. 32.4 in W&C, if your collection angle has been determined using standard specimens such as NiOx or NIST standard specimens, which we describe below. If every parameter looks OK, you can return to the main dialog by clicking the 'OK' buttons.
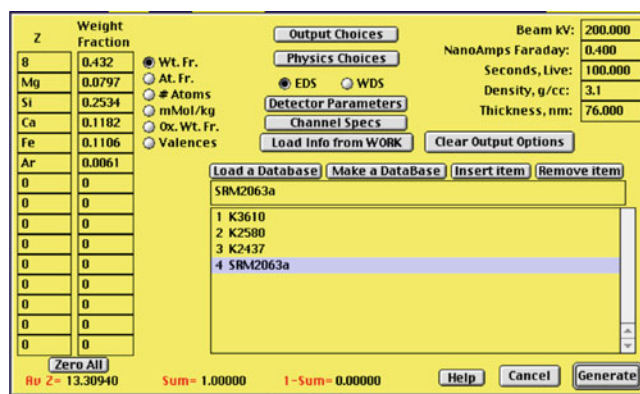

Fig. 17.8 Screen shot of the main dialog for thin-specimen spectrum generation in DTSA

If you prefer to change the energy dispersion (eV/channel), click the 'Channel Spec' button to select the eV per channel and the number of channels (Fig. 17.9c). For a typical X-ray spectrum from a thin specimen, 10 eV per channel with 2,048 channels are good values. Then, click 'OK' to return to the main dialog.

Specimen Information: Specific information about your specimen should be input in the main dialog. All you need to input is the constituent elements and their compositions, the specimen density and its thickness. For element information, either an atomic number such as '8' or an atomic symbol such as 'Mg' can be used. You can also select several different units for compositions. Note that the spectrum simulation does not require the density value for the bulk target (one of the major differences between the bulk and thin targets simulations). As an example, in Fig. 17.8, information about the NIST standard reference material (SRM) glass, thin film, 2063a is shown. This specimen has had its composition, density and thickness already certified by the NIST SRM program – hence by the US government! You can also save the input information to a Database in DTSA.

Experimental Information: Experimental conditions can also be set up in the main dialog (Fig. 17.8). Only three parameters are required for the spectrum simulation: the incident electron energy, probe current, and acquisition time.

Physics Choice: The last parameters you need to set up are related to the physics of X-ray generation. These parameters can be selected by clicking the 'Physics Choice' button available in the main dialog. An independent sub-dialog appears, as shown in Fig. 17.10. In this sub-dialog, models of the ionization cross-section for K-, L- and M-shells, and a cross-section model for continuum X-rays can be selected. In addition, you can also select scaling-factor values for each of the cross-section models. As we will describe in the following subsection, electron-induced X-ray signals are directly proportional to magnitudes of the cross-sections. Therefore, the physics settings chosen in this sub-dialog are very important to match with experimental

Chapter 17

Fig. 17.9 Screen shots of the dialogs for detector parameters (**a**), for detector geometry configuration (**b**), and for channel settings (**c**)
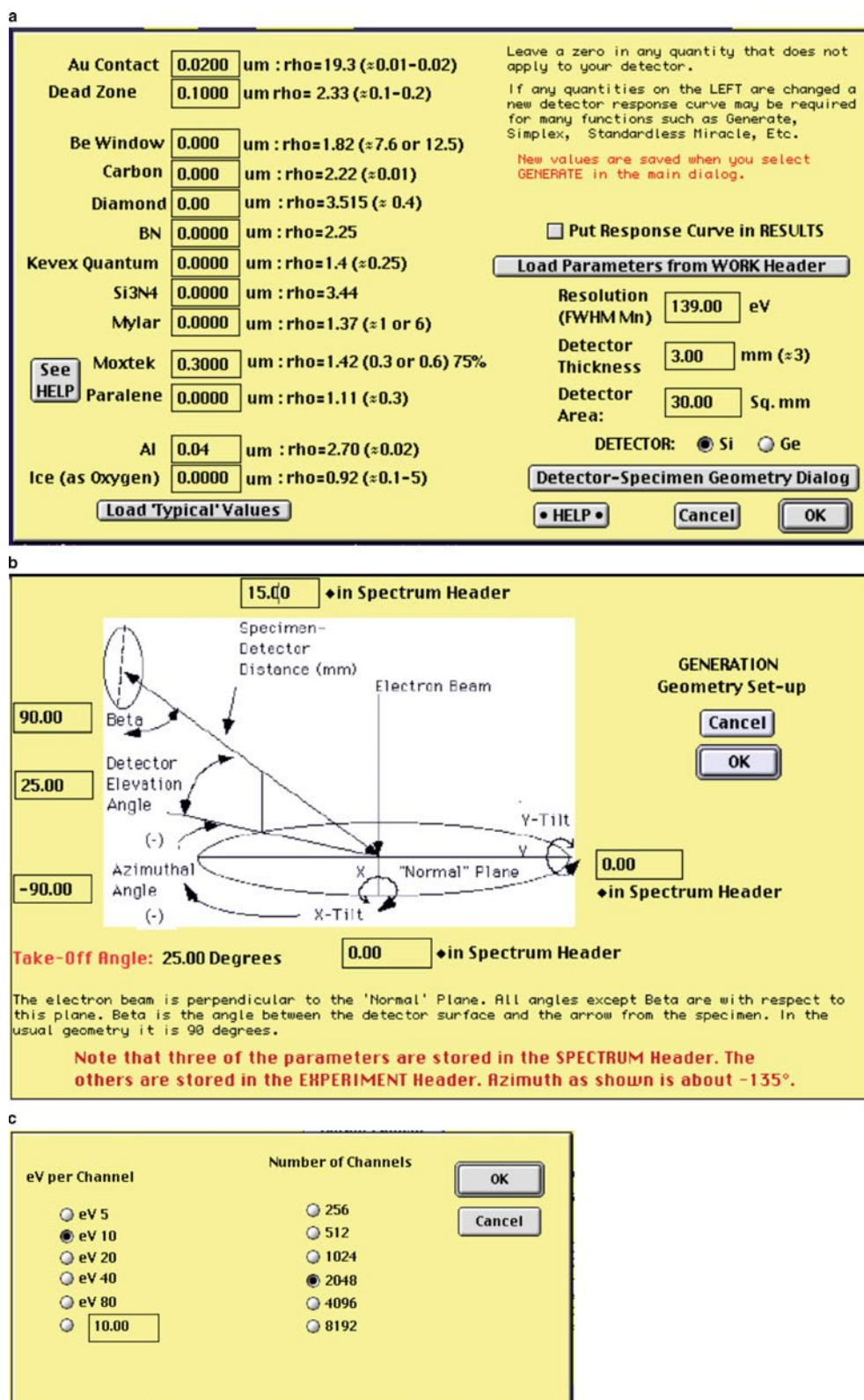
Fig. 17.10 Screen shot of the dialog for physics choice

spectra. However, unless you have any specific idea in terms of the selection of models and their scaling factor, or are very familiar with these models and concepts, you can leave them with default values or just click the 'Load Defaults' button. You can obtain preferential choices of the cross-section models with the corresponding scaling factors in determination of the ζ-factor method, as we explain in the next section. After setting up the physics choices, click the 'OK' button to return the main dialog.

Finally, an X-ray spectrum can be generated by clicking the 'Generate' button in the main dialog. Then, the generated X-ray spectrum is displayed as shown in Fig. 17.11a. This spectrum is ideal and clean, i.e., it has none of the spurious effects described in Chaps. 32 and 33 of W&C. At least, noise can be added to this spectrum, which is essential when you need to estimate analytical sensitivity. To add noise, you should select 'Math > Add Poisson Noise to Work' from the pull-down menu, and then another spectrum will appear with noise as a 'Results' spectrum, as shown in Fig. 17.11b. (Note: DTSA can display ten spectra simultaneously.) Yes, we add noise to the simulation rather than remove noise from the experimental data!

As we just described, one of the great advantages of DTSA is that you can go into the software dialog and try setting a whole different set of parameters. This approach allows you to see what effect the different values have on the generated spectrum of your particular specimen on which you are depending for your research. You'll immediately find which parameters are important and which do not affect your spectrum significantly. This aspect of spectrum simulation will of course help you in your general operation of the AEM. You'll soon learn which parameters you should select carefully and which you can generally leave to take care of themselves. Let's now explore further details of the spectrum simulation.

17.2.3 Details of X-ray Simulation in DTSA

A thorough understanding of X-ray generation and detection is useful if you need to interpret X-ray spectra acquired from a thin specimen and also for further quantitative analysis. Newbury et al. (1995; see their 2014 article for DTSA-II) reviewed a series of simulation procedures for an X-ray spectrum in DTSA in which the spectrum simulation for bulk targets is mainly featured. Unfortunately, we don't know of any detailed description available for the spectrum simulation for thin targets. So, here, we explain step-by-step the details of the X-ray spectrum simulation for a thin target.

Characteristic X-ray Generation: In a bulk sample, the generation of characteristic X-rays is a very complicated series of phenomena and many aspects need to be taken into account for spectrum simulation. In contrast, the X-ray generation process in a thin specimen is much more straightforward. In a thin specimen, we can make a few key assumptions:

- The energy loss of the incident electrons is negligible, because the energy loss can be as low as only 3 % (in up to 500-nm-thick specimens) even at 100 kV.
- Electron backscattering loss is also ignored since most of the scattering events in TEM are forwardscattering.
- The depth distribution of X-ray production is unity.

With these approximations the characteristic X-ray generation in a thin specimen can be simplified to be proportional to the mass thickness (ρt) and the characteristic X-ray intensity I_c at a given beam current I_p and an acquisition time τ can be expressed as

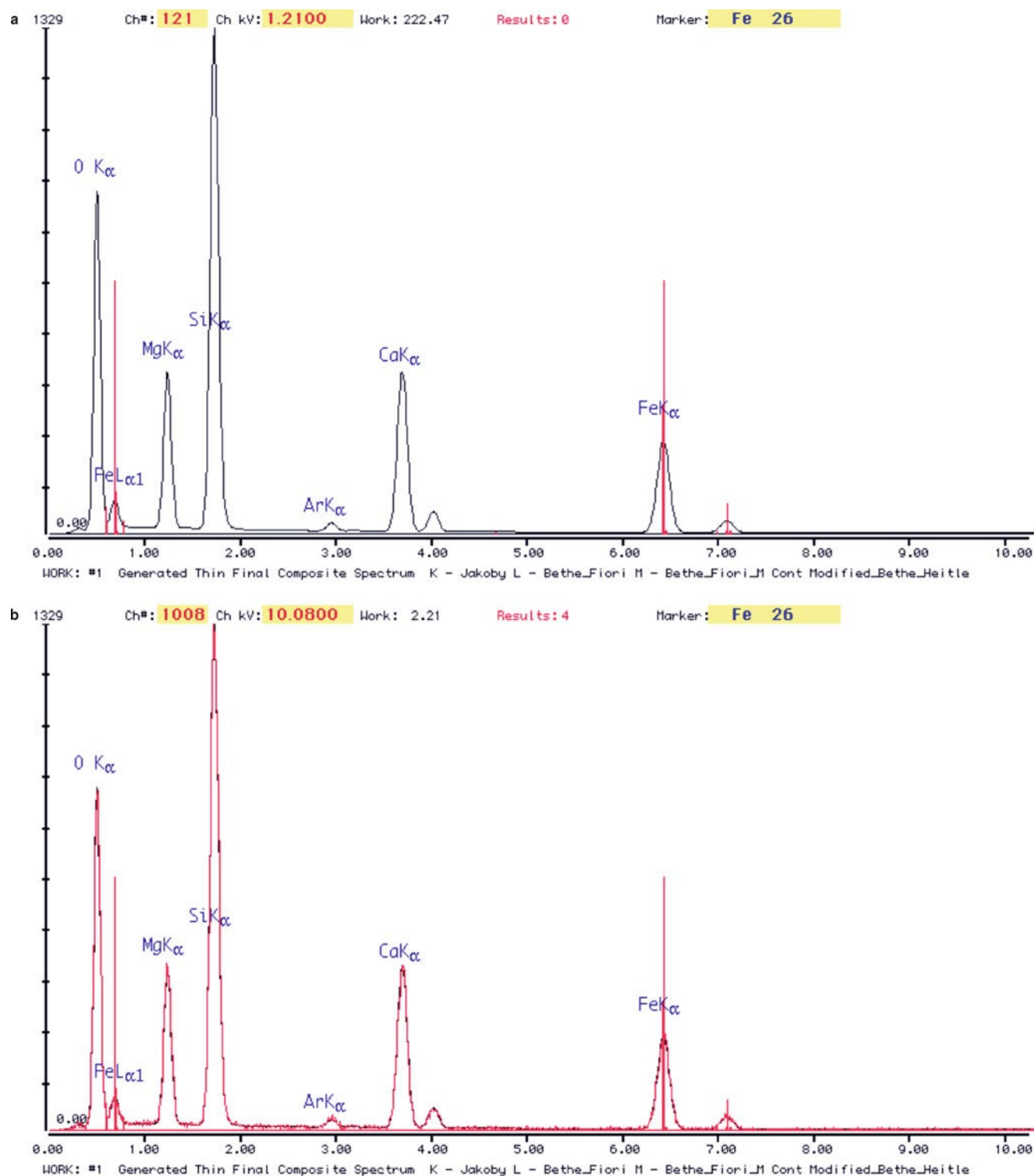$$I_C = \frac{s_i Q_i \omega a C N_v D_e}{A} \rho t \tag{17.11}$$

Chapter 17

Fig. 17.11 Example of simulated X-ray spectra from the NIST SRM2063a thin specimen. **a** Noise-free ideal spectrum. **b** Spectrum with random noise
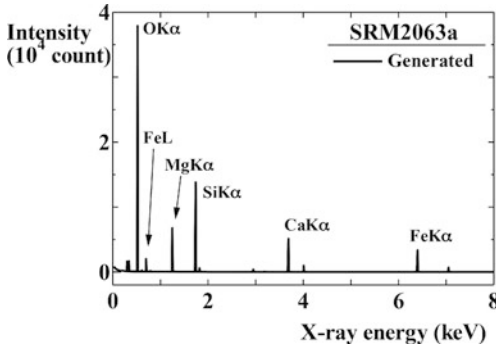
Fig. 17.12 Simulated result for a generated X-ray spectrum from the SRM2063a thin specimen

Fig. 17.13 Comparison between generated (*black*) and emitted (*red*) X-ray spectra from the SRM2063a thin specimen (**a**) and the X-ray signal loss in % due to X-ray absorption within the specimen, plotted against the X-ray energy (**b**)

where Q_i is the ionization cross-section, s_i is the scaling factor of Q_i, ω is the fluorescence yield, a is the line weight (or the relative intensity ratio), C is the weight fraction, A is the atomic weight, N_v is the Avogadro number, and D_e is the total electron dose defined as

$$D_e = N_e I_p \tau \tag{17.12}$$

where N_e is the number of electrons (electron counts) in a unit electric charge.

Continuum X-ray Generation: The continuum background of an X-ray spectrum can ideally be generated only by bremsstrahlung events. The intensity of the continuum X-ray I_b can be expressed similarly to Eq. 17.11 as a function of the X-ray energy E

$$I_b(E) = \sum_j \frac{s_C Q_{C,j}(E) C_j N_v D_e}{A_j} \rho t \tag{17.13}$$

where $Q_{c,j}(E)$ is the continuum X-ray cross-section at an X-ray energy E, s_c is the scaling factor of $Q_{c,j}$, and j is an index for each element included in the thin specimen. So, the continuum X-ray intensity is the sum of contributions from all the elements. In general, $Q_{c,j}$ is based on the classic description by Kramers as described in Eq.(35.7) in W&C. Especially for a thin specimen in an AEM, the angular distribution of continuum X-rays is not homogeneous, as was shown in Fig. 33.6 in W&C. We can handle this angular dependence of the continuum X-ray generation by including the detector elevation angle, and the specimen tilt angles in the proposed cross-section models of continuum X-ray generation in thin specimens.

The *generated* characteristic X-ray peaks are merged with the *generated* continuum X-ray spectrum in the first step of the spectrum simulation. Figure 17.12 shows an example of a *generated* spectrum from SRM2063a (thickness of 76 nm), simulated in the same microscope and for the experimental conditions in
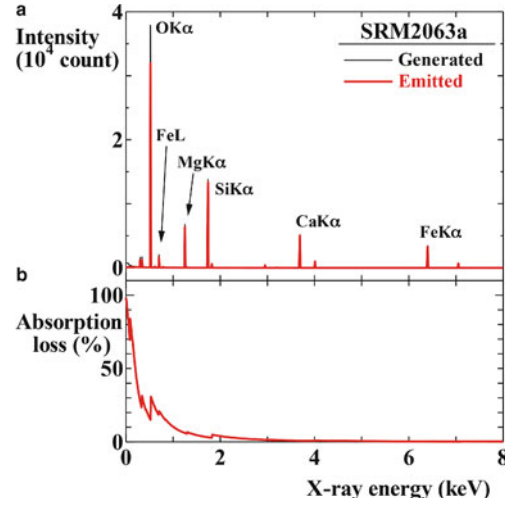
Fig. 17.11. Note that this *generated* spectrum is never seen in practice since the X-rays are not yet emitted from the specimen. In addition, the characteristic X-ray peaks are much sharper than a single channel width (10 eV/channel in this simulation). The actual generated peak width is narrower than 1 eV. You should note that intensities of all simulated spectra are normalized with the detector collection angle to make it easy to compare the spectra.

X-ray Emission after Being Absorbed in a Thin Specimen: Not all the generated X-rays are emitted from your specimen since some fraction of the generated X-ray is absorbed, even in a thin specimen. We can express the relationship between the generated and emitted X-ray intensities in a differential form:

$$\Delta I_{emit} = \Delta I_{gen} \exp\left[-(\mu/\rho)\rho z \operatorname{cosec} \alpha\right] \tag{17.14}$$

where ΔI_{emit} and ΔI_{gen} are the emitted and generated X-ray intensities from a small mass-thickness segment $\Delta(\rho t)$ at α depth of ρz from the incident surface, respectively, and α is the X-ray take-off angle. In DTSA, the total emitted X-ray intensity is calculated by integrating all the X-ray intensities, including absorption, in the individual segments. We compare an emitted spectrum from SRM 2063a (red solid line) with a generated one in Fig. 17.13a. Fig. 17.13b, the fraction of X-ray absorption is plotted in percent as a function of the X-ray energy. Despite the very thin SRM 2063a specimen (only 76 nm), you can see that a considerable fraction of the X-rays generated at energies lower than 1 keV (soft X-rays) is absorbed into the specimen and not emitted. For instance, more than 30 % of the generated O Kα is not emitted

Chapter 17
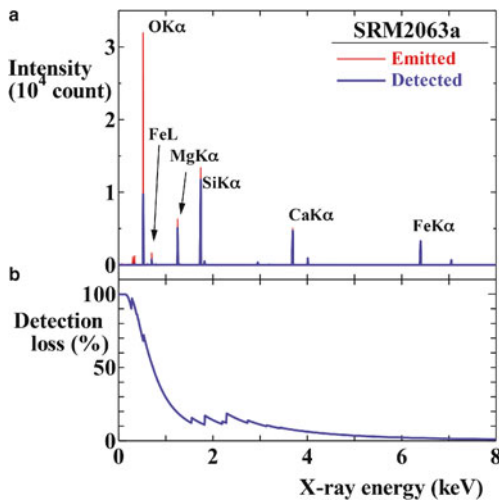
Fig. 17.14 Comparison between emitted (*red*) and detected (*blue*) X-ray spectra from the SRM2063a thin specimen (**a**) and the X-ray signal loss in percent due to absorption in the detector, plotted against the X-ray energy (**b**)

Fig. 17.15 Comparison of X-ray spectra from the SRM2063a thin specimen before (*blue*) and after (*orange*) broadening due to the detector electronics (**a**) and the detector energy-resolution plotted against the X-ray energy (**b**)

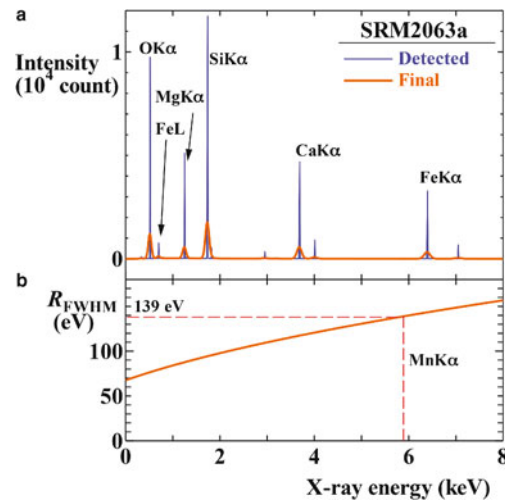from the film due to absorption. In contrast, X-ray absorption is negligible for X-rays >2 keV.

Influence of the Detector Collection Angle: X-rays are emitted radially into a 4π steradian, spherical space. However, only a small portion of the X-rays can be collected, depending on the XEDS detector geometry, defined by the collection solid angle Ω. As we described earlier, only 0.1~3 % of all the emitted X-rays are collected in commercial AEMs unless you use the latest SDDs with large solid angles. The X-ray intensity collected by the detector can be expressed as:

$$I_{col} = I_{emit}\left(\frac{\Omega}{4\pi}\right) \tag{17.15}$$

As we also mentioned above, the background intensity is dependent on the take-off angle of the detector, which is included in the cross-section models of the continuum X-rays.

X-ray Absorption and Transmission in the XEDS Detector: The collected X-rays reach the active area of detector crystal through the detector window. In this process, the low-energy soft X-rays may be absorbed by your detector window and by any contamination layers in front of the window. In addition, higher-energy, hard X-rays may transmit through the detector crystal, especially if it is a Si(Li) crystal or an SDD crystal. We describe the loss of X-ray due to the window absorption and crystal transmission in terms of the detector efficiency ε, which is given as Eq. 35.15 in W&C. We can express the detected X-ray intensity as:

$$I_{det} = I_{col}\varepsilon \tag{17.16}$$

In Fig. 17.14a, we compare the detected spectrum (blue solid line) with the emitted spectrum. As we mentioned above, the intensities of both spectra were normalized with the collection angle $\Omega/(4\pi)$. In Fig. 17.14b, detection losses due to window absorption and crystal transmission are plotted (in percent) as a function of the X-ray energy. Again, you can see that the soft X-rays below 2 keV are reduced significantly for a Si(Li) detector (even with an atmospheric ultra-thin window (UTW)). The O Kα intensity drops to only ~25 % of the generated intensity due to absorption in the specimen and losses during detection. If your detector window is contaminated with carbon and ice, further intensity loss will occur.

Influence of Detector Electronics: The peaks of detected characteristic X-rays are still very sharp in the detected spectrum (Fig. 17.14). However, these sharp peaks are blurred by the X-ray detection process and the detector electronics. This blurring is proportional to the X-ray energy and expressed as

$$R_{FWHM}(E) = \sqrt{2.5(E - E_{MnK\alpha}) + R_{FWHM}(MnK\alpha)^2} \tag{17.17}$$

where $E_{MnK\alpha}$ and $R_{FWHM}(MnK\alpha)$ are the energy and detector resolution at the Mn Kα peak. The spectrum blurred by the detector electronics (orange solid line) is superimposed on the detected spectrum at the top in Fig. 17.15. Fig. 17.15b, the energy resolution $R_{FWHM}(E)$, calculated using Eq. 17.17, is plotted against the X-ray energy. Although the characteristic peak intensities remain the same, you can see that the height of each peak (hence the peak-to-background ratio) is significantly reduced due to the blurring. With such blurring, DTSA finally produces a simulated X-ray spectrum which has the familiar shape we usually see on our computer display.

Fig. 17.16 Screen shot of the dialog for output choice
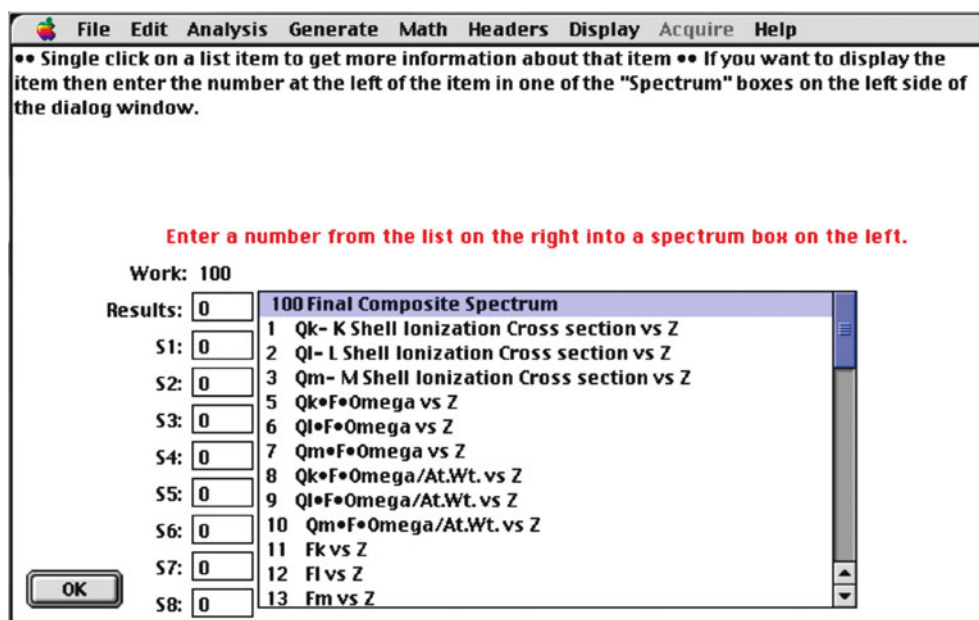
Using DTSA, you can simulate an X-ray spectrum at each detection step. In the main dialog for thin-specimen spectrum generation (Fig. 17.8), click the 'Output Choice' button and then you can select appropriate indices for desired outputs in the output choice dialog (Fig. 17.16).

17.2.4 Application 1: Confirmation of Peak Overlap

Once you understand the X-ray simulation process in DTSA, you can apply the spectrum simulation feature for your specific research needs. You should perform the spectrum simulation before doing the experiment but after reading this chapter and those in W&C! (Then read the chapters again and repeat the process!) In the rest of this section, we will introduce several useful applications of spectrum simulation.

The first application you should always carry out is the confirmation of the energy positions of all the characteristic X-ray peaks from your specimen. As described in Sect. 34.3 of W&C, you can confirm any peak overlaps simply by the spectrum simulation in DTSA. Figure 17.17 shows a simulated X-ray spectrum with a selected energy range of 1–4 keV from MoS_2, which is one of the famous '*pathological overlaps*'. To confirm the peak energy positions, KLM markers of the Mo L and S K line families are also shown in Fig. 17.17. You can see that the Mo Lα peak is superimposed on the S Kα peak. In addition, the S Kβ peak lies between the minor Mo Lβ_4 and β_3 peaks as well. You can easily confirm whether the peak at 2.3 keV is the Mo L or S Kα by checking the presence of the Mo Kα line at 18 keV. However, the

major question is "Is it possible to identify the existence of a S Kα peak in the presence of Mo?". The answer is "yes" – if a sufficient amount of S is contained in the analyzed region. You can confirm the S presence by comparing (1) the Mo K/L intensity ratio from a pure Mo standard thin specimen and (2) the energy resolution of the peak at 2.3 keV. In contrast, if you try to identify S with a low amount in the presence of Mo, the situation becomes much harder. (Look at the chapter on spectral imaging.)

> **Overlapping Peaks**
>
> If there are several characteristic peaks at very similar energy ranges, the peaks might overlap one another and it is important to know this before you carry out your experiments: DTSA can help.   ◄

If your specimens are not self-supported (such as nanoparticles or FIB lift-out coupons) you must use supporting grids. Selection of the supporting grids is another important task prior to any practical experiments. Again, you can evaluate suitable supporting grids with the aid of a spectrum simulation. For example, a simulated spectrum from HfO_2 is shown in Fig. 17.18. HfO_2 is used in optical coatings and in DRAM capacitors as a high-k dielectric. It has recently attracted attention as a good candidate for the gate oxide in field-effect transistors to replace current silicon oxides. Therefore, HfO_2 is often analyzed in a TEM, either on its own and as one of the components in a semiconductor device. In Fig. 17.18, the KLM markers of Cu and Mo (both are common support-grid materials) are also shown. Both the Cu Kα and Kβ lines overlap with the Hf L peaks. Obviously, you can see that the (more popular) Cu grids
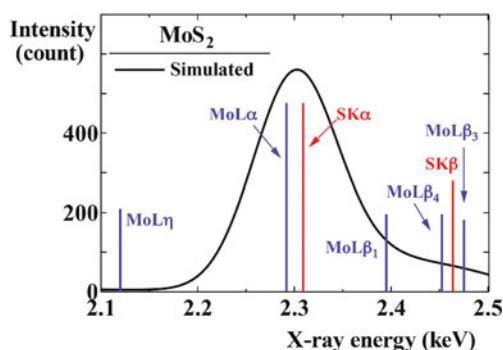
Chapter 17

Fig. 17.17 Simulated X-ray spectrum with a selected energy range of 1–4 keV from MoS_2, showing *pathological overlaps* between the Si Kα (*red*) and Mo Lα (*blue*) peaks
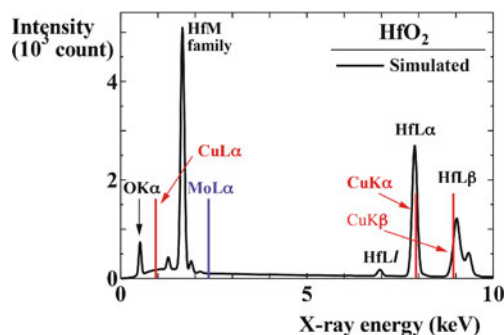

Fig. 17.18 Simulated X-ray spectrum from HfO_2 with KLM markers for Cu and Mo. Since the Hf L-line family is superimposed on the Cu L-line family, a Cu grid is not advisable for X-ray analysis of materials containing Hf

should not be your primary choice for XEDS analysis of Hf. Instead, you can use a Mo grid to mount a FIB-cut specimen from a semiconductor device which contains HfO_2. In addition to the grid materials, you may check other X-ray peak overlaps with Ga and also with protective deposition materials such as W or Pt.

17.2.5 Application 2: Evaluation of X-ray Absorption into a Thin Specimen

We have stressed that X-ray absorption, even in the thinnest specimens, may not be negligible for lower energy X-rays. As we explained in Eq. 17.14, how X-ray absorption affects your spectrum depends on the thickness, density, and mass absorption coefficient of the specimen and the X-ray take-off angle. You can evaluate the expected X-ray absorption of your specimen using the spectrum simulation in DTSA before you start your actual experiments.

Figure 17.19a shows three spectra simulated at different thicknesses of 50, 100, and 300 nm of NiAl intermetallic compound in a 200-kV-instrument with an X-ray take-off angle of 25º. To ensure a fair comparison, we have normalized these spectra to the maximum peak intensity of the Ni Kα line. As the specimen thickness increases, you can see that the peak heights of the Ni Lα and Al Kα lines are relatively reduced. The absorption loss of the Ni Kα, Ni Lα, and Al Kα lines are shown as a function of the specimen thickness in Fig. 17.19b. For calculation of the absorption loss, we used an X-ray take-off angle of 25º. We can calculate the MAC of the individual X-ray lines in the specimen by the weighted mean of the individual MAC values of the constituent elements:

$$(\mu/\rho)_{sp}^{X} = \sum_{j} C_j (\mu/\rho)_j^{X}$$

$$(17.18)$$

In Table 17.4, the MACs of the Ni Kα, Ni Lα and Al Kα lines in Ni, Al and NiAl are summarized. The red dashed line in Fig. 17.19b indicates a 10% loss of the total intensity due to absorption in the specimen. When more than 10% of absorption occurs, the absorption correction may be required for good quantitative analysis. We define the specimen thickness which causes 10% absorption loss as the critical thickness. As shown in Fig. 17.19b, the critical thicknesses for the Al Kα and Ni Lα are 54 and 97 nm, respectively, again confirming the dangers of absorption from lighter elementss, even in thin films.

The absorption path length is dependent on the X-ray take-off angle α and given as $t\cosec\alpha$ for a specimen thickness t. However, the path length varies with the specimen tilt-angle. You can reduce the absorption path if you tilt your the specimen toward the XEDS detector, or increase it by tilting away. If we define the tilt angle toward the detector as θ, we can express the total take-off angle as $\alpha+\theta$. Fig. 17.20 shows X-ray spectra from a 100 nm thick NiAl film simulated under conditions of no-tilt, +15º tilt (toward the detector, the total take-off angle: 40º) and −15º tilt (away from the detector, the total take-off angle: 10º). Although the peak intensity of Ni Kα is almost unchanged, the peaks of both the Ni Lα and Al Kα vary significantly with the tilt conditions. Therefore, you can control the absorption path length, i.e., the absorption effect, to some degree, by tilting your specimen. In addition, you should know the proper configurations of the specimen-detector geometry in your instrument, if you still insist on tilting your specimen for analysis.

Be Aware

You decrease the *P/B* ratio as you tilt the specimen. ◄
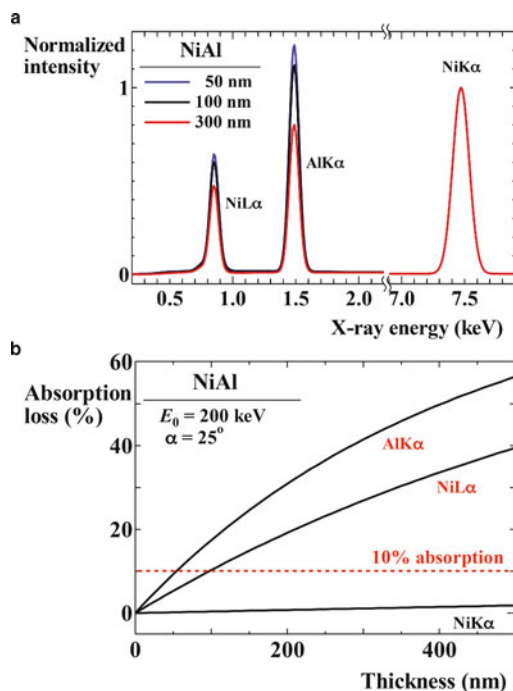
Fig. 17.19 a Comparison of three X-ray spectra simulated at different thicknesses of 50, 100, and 300 nm of Ni_3Al intermetallic compound in a 200 kV instrument with an X-ray take-off angle of 25°. These spectra were normalized by the maximum peak intensity of the Ni Kα line. **b** The signal losses (%) of the Ni Kα, Ni Lα and Al Kα lines due to the absorption into the specimen, plotted against the specimen thickness

Table 17.4 Summary of MAC values of the Ni Kα, Ni Lα and Al Kα lines in Ni, Al and NiAl intermetallic compound. The MAC values in the pure elements are calculated from Heinrich's formula (Heinrich 1987) and those in NiAl are obtained from Eq. 17.18 using the values in the pure elements

Absorber	MAC (m²/kg)		
	Ni Kα	Ni Lα	Al Kα
Ni	6.0	181.1	454.3
Al	6.1	179.8	39.7
NiAl	6.0	180.8	323.8

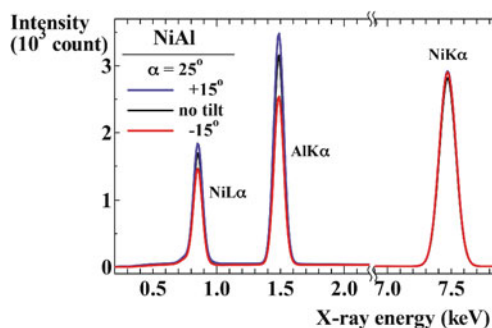**Fig. 17.20** Comparison of three X-ray spectra of NiAl simulated at different tilt angles of –15°, 0°, and +15°

17.2.6 Application 3: Evaluation of the AEM-XEDS Interface

Using DTSA, you can also simulate an X-ray spectrum in unusual conditions – sometimes these conditions may be unrealistic. In Sect. 33.3 of W&C, we discuss why an XEDS detector is mounted on the incident-beam side of the specimen, despite the fact that characteristic X-rays are emitted uniformly over a 4π steradian sphere. The major reason for this choice is the angular dependence of the continuum X-ray emission: the background-intensity distribution is maximized in the forward scattering direction and is reduced as the scattering angle increases toward backscattering directions. Using the DTSA spectrum simulation, you can confirm this angular dependence of the background intensity distribution. Figure 17.21a shows a comparison of two spectra from our standard NiOx test specimen, simulated at 200 kV with take-off angles of $\pm 70°$. Although the peak intensity of the Ni Kα line remains almost the same, you can see significant difference in the background intensity. As expected, the background intensity is much higher on the exit-surface side of the specimen, especially at lower energies.

Remember, the absorption-path length is the same in both geometries. In Fig. 17.21b, you can see the take-off angle dependence

of P/B of Ni Kα peak using the Fiori definition. The P/B value is much lower in the exit-surface side, and hence the higher take-off angle is desirable since we want to obtain higher P/B values. It's impractical to change the detector geometry in your microscope instrument (unless you have more money than sense). In contrast, you can easily vary the take-off angle in a DTSA simulation. Thus spectrum simulation is a very handy tool to support all your XEDS experiments.

17.2.7 Application 4: Estimation of the Detectability Limits

One of the most useful applications of the spectrum simulation is to evaluate detectability limits. This is why this particular application was the major motivation for the original development of DTSA (Fiori, Swyt 1989; Newbury et al. 1995). A commercialized software package (EELS Advisor for Gatan DigitalMicrograph) expands the concept of detectability evaluations to find experimental configurations for appropriate acquisition of EELS spectra and EFTEM elemental images. You can find the detailed procedures for detectability evaluation in the literature (e.g., Watanabe and Williams 1999). Here, we will show how you can evaluate three different parameters related to the analytical sensitivity, using the spectrum simulation.
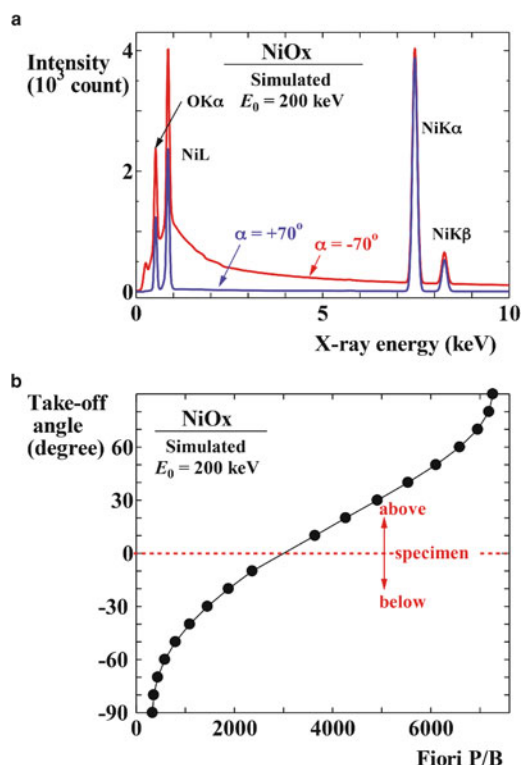
Chapter 17

Fig. 17.21 a A comparison of two spectra from a NiOx test specimen, simulated at 200 kV for take-off angles of ± 70°. **b** The take-off angle dependence of P/B of the Ni Kα peak (using the Fiori definition)

> **Look Before you Look!**
>
> It's obviously crucial to find out if you can actually detect what you are looking for, before you embark on specimen preparation and all the other time-consuming steps. ◄

Peak Detectability: After acquisition of an X-ray spectrum from your specimen, you may see that an element of interest only exhibits a small peak. In this situation, you must judge whether the small peak is actually visible or even detectable (is it just a fluctuation in the background noise?). Detailed descriptions of when a peak is visible or not can be found in Sect. 34.5 of W&C. Here we'll explore the peak visibility and detectability in practice using the spectrum simulation.

As an example, let's consider phosphorus detection in Fe. P is one of the impurities that can cause brittle failure in steels by segregating to grain boundaries. Therefore, the detection of small amounts of P (and other segregants) to GBs has long been one the major problems addressed by XEDS in the AEM. Figure 17.22a shows a typical spectrum simulated for a 100-nm-thick foil of Fe-0.15wt%P in a 200-kV instrument for an acquisition time of 100 s. From the spectrum, the peak (*P*) and background (*B*)
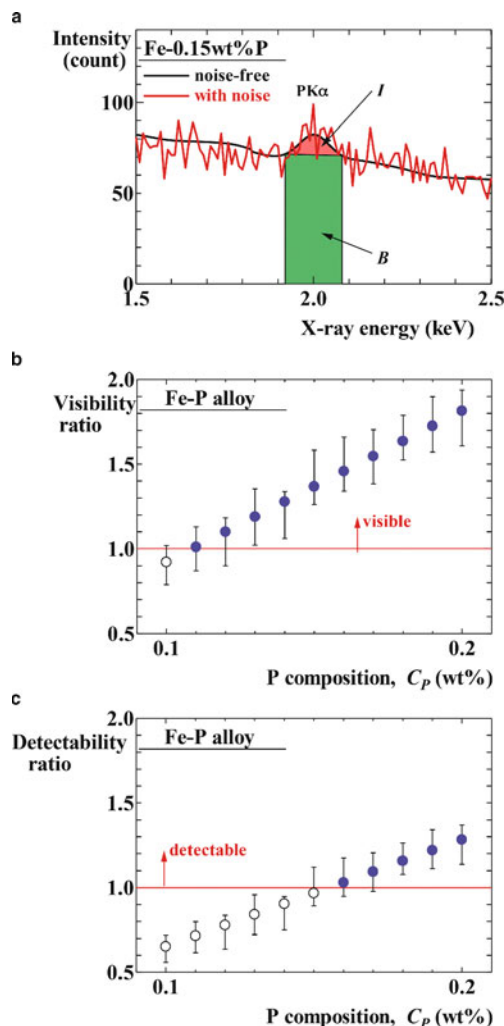

Fig. 17.22 a Comparison of two X-ray spectra from a 100-nm-thick Fe-0.15 wt%P simulated with and without noise in a 200 kV instrument for 100 s. Two highlighted regions indicate the net peak (I) and background (b) intensities. The peak visibility (**b**) and detectability (**c**) ratios of the P Kα line in Fe, plotted against the P composition C_p for 100-nm-thick films. The error bars represent the 3σ (99% confidence limit) range determined from 50 simulated spectra with different random noise conditions

intensities are measured in the same channel width, as shown in the shadowed areas in Fig. 17.22a. Then, the net peak intensity (*I*) is determined by subtracting *B* from *P*. As we described in Sect. 34.5 of W&C, if the net peak intensity exceeds $3\sqrt{B}$, the peak is visible with a 99% confidence limit (3σ). In addition, when $I > 3\sqrt{2B}$ (*slightly stricter than the visibility limit*), the peak is detectable as mentioned in Sect. 36.4B of W&C. Let's denote $I/3\sqrt{B}$ and $I/(3\sqrt{B})$ as the visibility and detectability ratios, respectively. So, if $I/(3\sqrt{B})$ or $I/(3\sqrt{2B}) > 1$ in terms of the P Kα peak, then the peak is visible and the phosphorus is detectable in Fe, respectively. Figures 17.22b, c show the visibility and detectability ratios of the P Kα line in Fe, plotted against the P composition (C_p) for 100-nm-thick films. As you can see, the

P Kα peak is visible at $C_P = 0.11$wt% and becomes detectable at $C_P = 0.16$wt%.

These simulated results are calculated assuming ideal conditions and could be very different from realistic situations since we have not included any noise associated with signal generation and detection. In DTSA, we can add such random noise to simulated spectra, based on Poisson counting statistics. In Fig. 17.22a, we show another simulated spectrum with random noise as a red line. Obviously, it becomes harder to recognize such a small peak under the noise, which is more similar to practical cases, and hence the peak visibility and detectability are degraded when we add noise to the spectrum simulation. We determined the 3σ range of the peak visibility and detectability from 50 simulated spectra with different random noise conditions for each P composition and these are shown as error bars in Fig. 17.22b, c. The results from the noise-free spectra appear close to the average of those with random noise.

You should note that the above definitions for the peak visibility and detectability are approximately equivalent to the decision (L_c) and detection (L_d) limits in Currie's definitions for the analytical sensitivity limits (described with Eqs. (36.16)–(36.20) in Sect. 36.4C of W&C). Furthermore, the above visibility limit also corresponds to the visibility of a 1D image (*i.e., the spectrum!*) in the Rose criterion. You should be able to work out how these definitions are related to one another in some degree.

Minimum Mass Fraction (MMF): The detectability limit we described above is essentially the same as the MMF, which is the minimum detectable composition. You can calculate the MMF value from the peak and background intensities of a standard specimen with a known composition using the Goldstein–Romig–Michael (GRM) equation (Eq. 35.15) first discussed in Sect. 36.4B of W&C. The MMF values for P in Fe, determined from simulated X-ray spectra of Fe-5wt%P by the GRM equation, are plotted against the specimen thickness in Fig. 17.23. The simulation parameters are same as those in Fig. 17.22 (accelerating voltage: 200 kV and acquisition: 100 s) and the error bars are determined from 50 spectra simulated, with noise, at each thickness condition. As you can see, in comparison with the detectability evaluation shown in Fig. 17.22c, the error bars are much smaller. This is because the C_P(MMF) values are calculated using simulated spectra with the high P composition. The calculated C_P(MMF) value decreases as the specimen thickness increases simply because the X-ray signal increases. In the 100-nm-thick film, C_P(MMF) approaches ~0.16 wt% under these conditions. Therefore, the C_P(MMF) value calculated using Eq.(36.15) agrees well with the detectability limit determined from simulated spectra with trace amounts of elements.

Minimum Detectable Mass (MDM) or Minimum Detectable Atoms (MDA): Another expression of the analytical sensitivity is the MDM, which is more conveniently defined as the minimum number of atoms detectable in the analysis volume in your thin specimen in the AEM, i.e., MDA. As we already
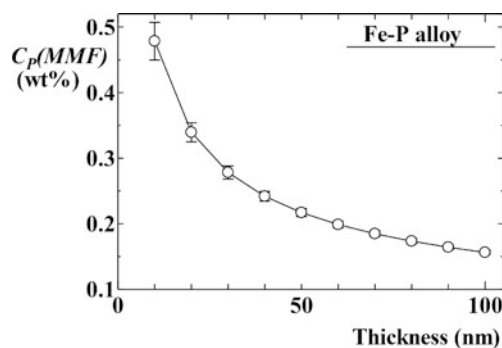

Fig. 17.23 MMF of P in Fe, determined from simulated X-ray spectra of a thin foil of Fe-5 wt% P using the GRM equation, plotted against the specimen thickness

described in Sect. 36.4D of W&C, the MDA in AEMs is now at or approaching the single atom level as we show below. This value is better than any other analysis technique. (Atom-probe microscopy is the only competition.)

To calculate the MDA values by translating from the MMF, you need first to calculate the analyzed volume. To do this, you need to know your probe size and your specimen thickness. Figure 17.24a shows the analyzed volume of Fe determined based on the Gaussian broadening model (see next section) for LaB$_6$-AEM (probe size, $d = 10$ nm), FEG-AEM ($d = 2$ nm) and aberration-corrected (AC) FEG-AEM ($d = 0.2$ nm), plotted against the specimen thickness. If you were to analyze a thinner region, the incident probe size becomes the dominant factor rather than the beam broadening. This smaller analyzed volume is more significant if the AC instrument is used. However, the benefit of using an AC instrument is obviously degraded when you are analyzing specimens thicker than ~50 nm. So if you've paid for an expensive AC AEM, don't waste time putting thick specimens in it!

You can convert the analyzed volume to the total number of atoms using basic crystallographic information. For example, Fe has a bcc structure with 2 atoms in the unit cell (i.e., the unit volume per atom can be given by (a^3)/2, where a is the lattice parameter). Then, by multiplying the atomic fraction of the MMF value (you have to convert the MMF value (in wt%) to the atomic fraction), the MDA can be determined. The MDA of P in Fe translated from the MMF in three different instruments is shown in Fig. 17.24b as a function of the specimen thickness.

Single-atom AEM!

We can identify single atoms! (See the paper by Lovejoy et al. 2012) ◄

Despite having a poorer MMF (higher mass fraction) in thinner regions, the MDA value is improved as the specimen thickness decreases. According to these results, only ~20 P atoms are de-
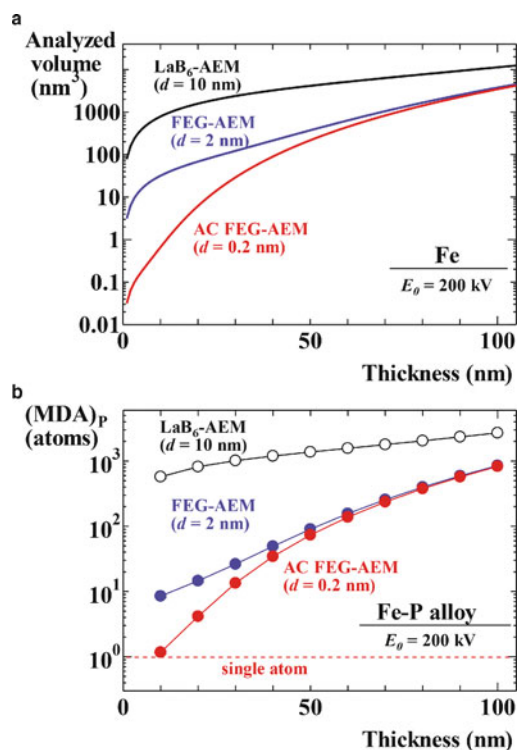
Fig. 17.24 **a** Analyzed volume of Fe determined based on the Gaussian broadening model for LaB_6-AEM ($d = 10$ nm), FEG-AEM ($d = 2$ nm) and AC FEG-AEM ($d = 0.2$ nm), plotted against the specimen thickness. **b** The MDA of P in Fe calculated from the MMF in Fig. 17.23 with the analyzed volume size

tectable by using the FEG-AEM under these specific conditions. This value may be improved to *a single-atom level* in the AC instrument. If you use longer acquisition times or the X-ray collection efficiency is improved with better detector geometries (e.g., larger collection angles), it's possible that the MDA value might be further improved.

17.3 The ζ-factor Method: a New Approach for Quantitative X-ray Analysis of Thin Specimens

In Chap. 35 of W&C, different approaches to quantitative X-ray analysis are described for thin specimens in the AEM. Since the development of the ratio method by Cliff and Lorimer (1995), this particular method has become the standard approach and is widely used due to its simplicity. Unfortunately, even in thin specimens, X-ray absorption may need to be corrected for quantification and the simple Cliff–Lorimer approach is found wanting. As we've noted many times, X-ray absorption is more serious in some materials than others, especially if lighter elements are present, and then the accuracy of quantification is

worsened. Furthermore, the X-ray absorption correction for thin specimens in AEM is harder than that for bulk samples in SEM/EPMA because you need to know some essential prior information about the specimen thickness and the density at every individual analysis point.

Several methods are proposed for thickness determination in Chap. 36 of W&C. However, these thickness measurements need to be performed independently of the X-ray analyses and doing this may introduce additional errors, which could also be an additional limiting factor for quantitative X-ray analysis. So, the conclusion we draw is that although applying the Cliff–Lorimer ratio method is straightforward, it cannot achieve the necessary levels of accuracy and precision in quantitative X-ray analysis in many thin specimens. The ζ-factor method is a new and improved quantitative procedure for thin specimens that overcomes some of the limitations in thin-film X-ray analysis listed above by making local thickness determination an integral part of the process. In this section, we go into much greater depth than you saw in Sect. 35.5 of W&C and explore further details of the ζ-factor method.

17.3.1 Why Bother with Quantification?

Before explaining what quantitative X-ray analysis via the ζ-factor method is, it's worth asking whether such an involved quantification process is really required for materials characterization or not. In some cases, you'll find that elemental distributions can be determined, or a phase can be identified, by qualitatively analyzing a single spectrum. A typical example is shown in Fig. 33.11 in W&C. With prior knowledge of preferential elemental distributions, you can easily distinguish types of carbides in steel. If you can identify the different carbides, you often don't need further quantification.

As another example, a set of X-ray intensity maps of Pb L and O K lines taken from a triple point of a Pb-based oxide $Pb(Mg_{1/3}Nb_{2/3})O_3$-35 mol%PbTiO$_3$ is shown in Fig. 17.25a along with an ADF-STEM image (Gorzkowski et al. 2004). From these elemental maps, you might infer that both Pb and O are depleted along the boundaries constituting the triple point. Using these elemental maps, quantification was performed by the ζ-factor method and a different set of composition maps of Pb and O obtained, as we show in Fig. 17.25b. In addition, a thickness map was obtained through the ζ-factor quantification process. As we inferred from the elemental map, depletion of O is confirmed at the boundaries and the triple point. However, quantification shows that Pb is actually segregated to the triple point, which is contradictory to the original conclusion from the elemental map.

According to the thickness map determined by the ζ-factor method, the thickness decreases along the boundaries and at the triple point, which reduces the X-ray intensity of the Pb L line. Therefore, the discrepancy between the qualitative elemental and
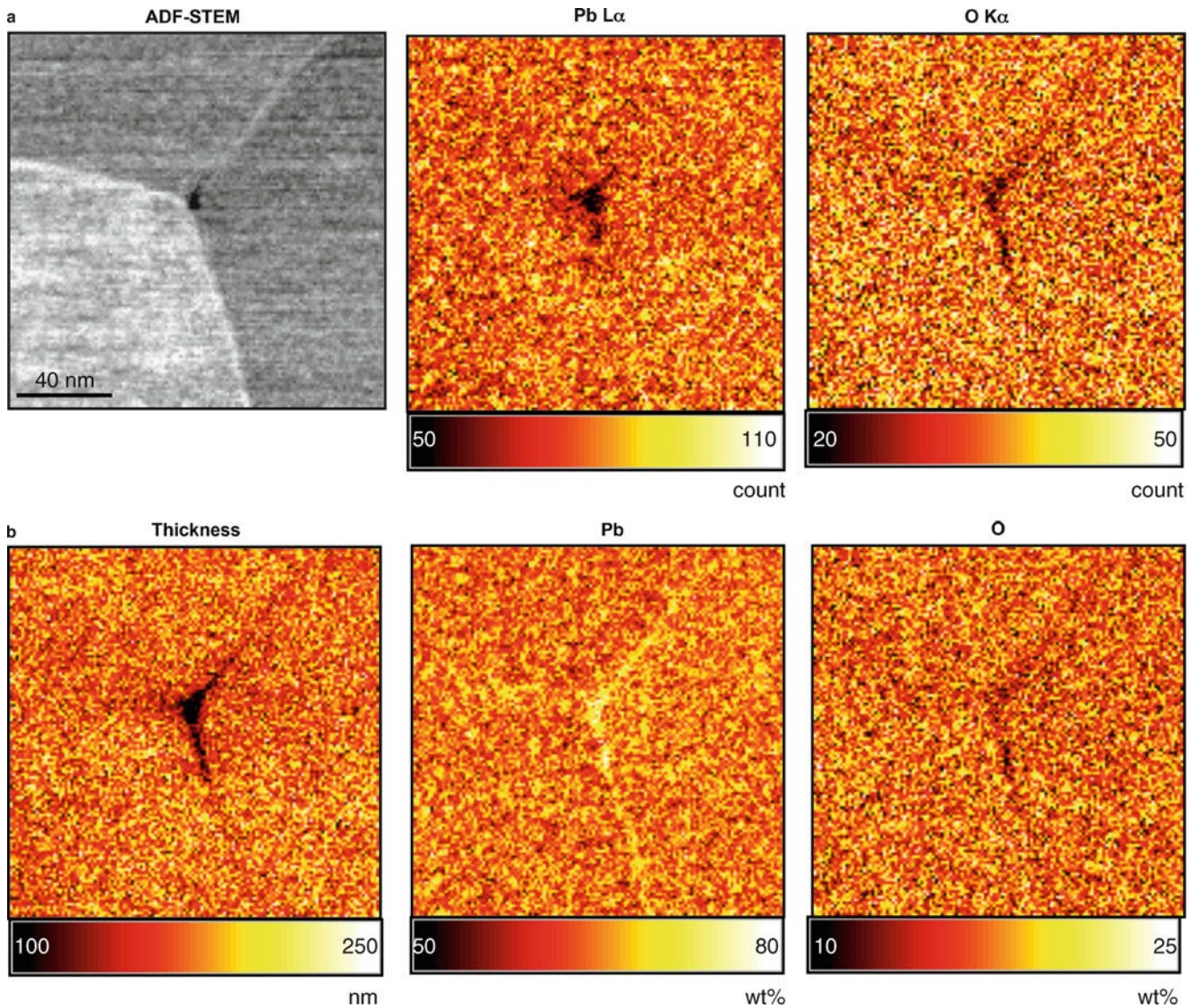
Fig. 17.25 **a** Set of X-ray intensity maps of Pb L and O K lines taken from a triple point in a Pb-based oxide $Pb(Mg_{1/3}Nb_{2/3})O_3$-35 mol%$PbTiO_3$ and an ADF-STEM image. **b** A set of composition maps of Pb and O with a specimen thickness map quantified by the ζ-factor method (Gorzkowski et al. 2004)

quantitative compositional maps of Pb has arisen. The thickness reduction along the boundaries constituting the triple point was caused by preferential thinning during specimen preparation by FIB. From this example, you should conclude that qualitative analysis, or simply looking at X-ray intensity changes may result in wrong conclusions. Quantification is an essential process for materials characterization! You will be ready to use quantification procedures via the ζ-factor once you understand and agree with this example!

17.3.2 What Is the ζ-factor?

In a thin-film specimen, the measured characteristic X-ray intensity I is proportional to the mass thickness ρt and the composition (weight fraction) C unless the generated X-ray signals are affected by absorption and fluorescence. We can establish the following relationship between the mass thickness and the measured X-ray intensity by normalizing with the total electron dose D_e (i.e., the number of electrons hitting the analysis region during X-ray acquisition)

$$\rho t = \zeta_A \frac{I_A}{C_A D_e} \tag{17.19}$$

Chapter 17

where ζ_A is a proportionality factor to connect I_A to ρt and C_A. If X-ray absorption and fluorescence are negligible because the specimen is thinner than the critical thickness, the generated characteristic X-ray intensity can theoretically be described as

$$I_A^g = N_v \frac{Q_A \omega_A a_A}{A_A} C_A \rho t D_e \qquad (17.20)$$

where N_v is Avogadro's number, Q_A is the ionization cross-section, ω_A is the fluorescence yield, a_A is the relative transition probability (i.e., the relative line weight) and A_A is the atomic weight. You should note that Eq. 17.20 is essentially the same as Eq. 17.11, which we introduced in the previous section – except for the scaling factor to adjust the absolute magnitude for ionization cross-section. By taking into account the X-ray collection efficiency terms such as the collection angle Ω relative to the whole sphere (4π) and the detector efficiency ε_A, we can express the measured X-ray intensity I_A as (see, e.g., Armigliato 1992)

$$I_A = I_A^g \left(\frac{\Omega}{4\pi}\right)\varepsilon_A = N_v \frac{Q_A \omega_A a_A}{A_A} C_A \rho t D_e \frac{\Omega}{4\pi}\varepsilon_A \qquad (17.21)$$

By comparing Eq. 17.19 with Eq. 17.21, the ζ factor can be defined as

$$\zeta_A = \frac{A_A}{N_v Q_A \omega_A a_A \left[\Omega/(4\pi)\right]\varepsilon_A} \qquad (17.22)$$

The ζ factor contains terms for both X-ray generation and detection. In other words, the ζ factor is equivalent to the atomic-number correction term (Z) in the ZAF matrix correction procedure, which is widely employed for quantitative X-ray analyses of bulk samples in SEM/EPMA.

Since the same relationship described in Eq. 17.21 is true for any other element (e.g., B), we can derive the following equation by taking a ratio between elements A and B and rearranging:

$$\frac{C_A}{C_B} = \frac{A_A}{A_B}\frac{Q_B \omega_B a_B \varepsilon_B}{Q_A \omega_A a_A \varepsilon_A}\frac{I_A}{I_B} = \frac{\zeta_A}{\zeta_B}\frac{I_A}{I_B} = k_{AB}\frac{I_A}{I_B} \qquad (17.23)$$

Obviously, this relationship is exactly same as the definition of the Cliff–Lorimer ratio equation. Therefore, we find the relationship between the k factor and ζ factors is:

$$k_{AB} = \frac{\zeta_A}{\zeta_B} \qquad (17.24)$$

Once you know one of the ζ factors (e.g., from a reference element such as Si and Fe), you can determine other ζ factors from existing k-factor databases (e.g., Tables 35.1 and 35.2 in W&C). You should be clear that the ζ-factor method does not eliminate the widely used Cliff–Lorimer ratio method but expands the way we do quantitative X-ray analysis as described in the following sections.

17.3.3 Quantification Procedure in the ζ-factor Method

Fortunately, as we'll show, the quantification procedure in the ζ-factor method is quite simple. Since a similar relationship to Eq. 17.19 holds for element B independently, we can express C_A, C_B, and ρt as follows, assuming $C_A + C_B = 1$ in a binary system

$$C_A = \frac{\zeta_A I_A}{\zeta_A I_A + \zeta_B I_B} \quad C_B = \frac{\zeta_B I_B}{\zeta_A I_A + \zeta_B I_B} \quad \rho t = \frac{\zeta_A I_A + \zeta_B I_B}{D_e} \qquad (17.25)$$

Therefore, you can determine C_A, C_B, and ρt simultaneously by measuring their X-ray intensities. This approach can easily be expanded to any multi-component system as long as the assumption of $\Sigma C_i = 1$ is reasonable. Once you know the ζ factors, it is straightforward to determine compositions.

> **A Warning**
>
> You need to know the electron dose term D_e for accurate thickness determination: so beam current measurement is essential for quantification via ζ factors.   ◄

The need for this measurement is the major drawback to the ζ-factor method because measurement of the beam current is not always easy in TEM (unlike the SEM/EPMA). In some TEM instruments, it is straightforward to measure the in-situ beam current because there is an in-built Faraday cap (similar to SEM/EPMA). If you have an EELS detector on your AEM, you can also monitor the beam current by prior calibration of the detector readout system. Fortunately, if you have a modern instrument with a Schottky FEG source, the beam-current fluctuation over typical time periods for analysis should be less. In this case, the beam current does not need to be monitored frequently and can be calibrated easily through the readout from the viewing screen etc. We should also note that in the ζ-factor method, the mass thickness can be determined as shown in Eq. 17.25. To determine the absolute thickness, you need to know the specimen density at individual measured points. You can find out more about density determination in the Appendix.

Information about the mass thickness of your specimen at individual measured points is very useful when you need to correct for X-ray absorption, even in thin specimens. The absorption-correction term for a single X-ray line from a thin specimen is

$$A_A = \frac{(\mu/\rho)_{sp}^A \rho t \csc\alpha}{1 - \exp[-(\mu/\rho)_{sp}^A \rho t \csc\alpha]} \qquad (17.26)$$

where $(\mu/\rho)_{sp}^A$ is the mass absorption coefficient of the characteristic X-ray line in the specimen and α is the X-ray take-off
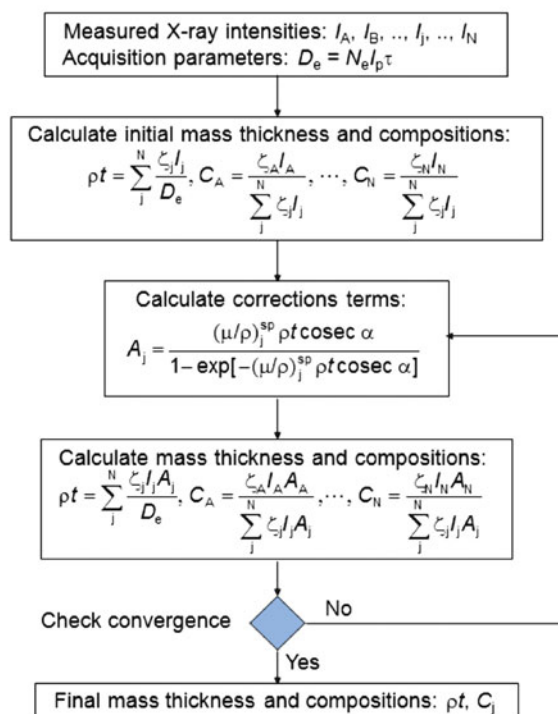
Quantification procedure in ζ-factor method

Fig. 17.26 Flow chart of the quantification procedure for the ζ-factor method with the X-ray absorption correction (Watanabe and Williams 2006)

Fig. 17.27 ζ-factors of *K* lines determined in a 200-kV JEOL JEM-ARM200CF, plotted against the X-ray energy. The *open circles* are the measured values from the SRM2063a glass thin-film; the *closed circles* indicate the estimated values by parameter optimization based on the measured values (Watanabe and Wade 2013)

angle. We incorporate this absorption-correction term into the ζ factor by multiplying it by the corresponding X-ray intensities in Eq. 17.25, via an iteration process. A complete flow chart for the quantification procedure via the ζ-factor method is summarized in Fig. 17.26. The calculation usually converges within five iteration steps. We should also mention that the local mass-thickness value is useful for the fluorescence correction on the very rare occasions when it is necessary. In the Appendix, you'll find the various steps in the error calculation for the iteration process summarized.

17.3.4 Determination of ζ factors

Similar to the Cliff–Lorimer k factors, the accuracy of your quantitative analysis is directly affected by the reliability of your ζ factors. You have to determine reliable ζ factors if you want reliable quantification. For the experimental determination of k factors, you should know that standard thin specimens with known composition (such as alloys and compounds) are required. Such standard thin specimens are also required for ζ-factor determination. However, unlike the *k-factor* determination, you can use pure element thin-films as standards for ζ-factor determination as might be expected from Eq. 17.19.

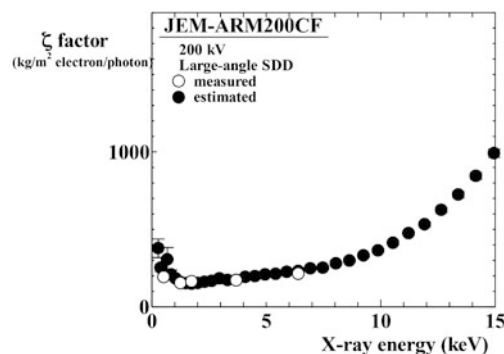Being able to use thin films of pure single-element materials is a major advantage and overcomes any limitations associated with thin-film standards since you can relatively easily fabricate pure-element thin films by evaporation, electron deposition or sputtering Such pure-element films are routinely available (in contrast to the tremendous difficulties to prepare multi-element, thin-film, standards with known compositions for *k*-factor determination). The only disadvantage you'll find is that the thickness of your standard film needs to be determined, prior to ζ-factor determination. However, if you do a bit of research you'll find that independent thickness determination is relatively easy in single-element, thin films.

The use of pure element thin standards expands the degrees of freedom for the ζ-factor determination. Unfortunately, you'll still find it very tedious to determine the many ζ factors from standard thin specimens when you need to analyze multi-element materials. This situation can be improved when you use the NIST-issued SRM 2063 or the re-issued 2063a glass thin-film standard. (Does your lab have such a sample?) Not only the compositions but also the thickness including the density of the SRM2063/2063a are well characterized. By measuring a single spectrum from the SRM2063/2063a, we can determine the ζ factors of the five major components. Then, based on the five ζ-factors determined from the SRM2063/2063a specimen, other ζ factors can be estimated by fitting uncertainty parameters such as absolute values of the ionization cross-section and window thicknesses of the detector.

Figure 17.27 shows the ζ-factors measured from a single spectrum of the SRM2063a specimen (open circles) in a JEM-ARM200CF aberration-corrected STEM at 200 kV with a large collection-angle XEDS detector, plotted against X-ray energy. The closed circles in Fig. 17.27 indicate a series of ζ factors estimated from the measured values by the parameter optimization. Although the NIST SRM2063a specimen is not available currently, similar types of materials can be utilized as standards for ζ-factor determination.

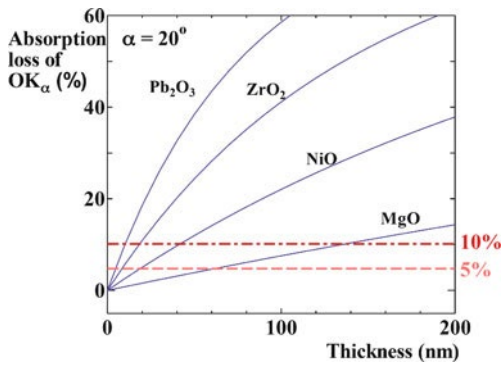**Chapter 17**

Fig. 17.28 Comparison of the absorption loss of the oxygen Kα intensity in various oxides, plotted against the specimen thickness. *Dashed* and *dot-dashed lines* represent 5% and 10% losses, respectively

17.3.5 Applications of ζ-factor Method

As we noted, there are several advantages to the ζ-factor over the Cliff–Lorimer ratio method. In this section, we'll highlight some of these advantages, which are mainly due to the availability of simultaneous thickness determination.

Light Element Analysis: Quantitative analysis of the many important materials systems that include light elements (e.g., the commercially important oxide, carbide and nitride systems) is always challenging. You know that X-ray emission from light elements below Si ($Z = 14$) in the periodic table is generally very low due to their low fluorescence yields. In addition, as we've now described several times, these light elements only produce soft X-rays (with energies below 2 keV) which are severely absorbed not only in the detector window but also in the specimen itself. The first effect reduces the detector efficiency and the second reduces the accuracy of our quantifications. Obviously this latter effect is more serious and has to be corrected! Figure 17.28 compares the absorption loss of the oxygen Kα intensity in various oxides, plotted against the specimen thickness. We calculate this absorption loss for an XEDS detector with the take-off angle of 20° using the following equation

$$L_A^X = 1 - \frac{1 - \exp\left[(\mu/\rho)_{sp}^X \rho t \csc \alpha\right]}{(\mu/\rho)_{sp}^X \rho t \csc \alpha} \tag{17.27}$$

The dashed and dot-dashed lines in Fig. 17.28 indicate the 5 and 10% absorption limits respectively. If the X-ray absorption exceeds 10%, the accuracy of quantification degrades correspondingly. If absorption reduces the accuracy that we reasonably expect from the quantification procedures, we need to correct for it. The oxygen Kα line is more severely absorbed in oxides with heavier elements. For example, 10% of the X-ray intensity is absorbed at ~20 nm in Pb_2O_3. It is rare that we can expect our specimens to be so thin.

Table 17.5 Comparison of measured compositions of Pb-based oxide with and without X-ray absorption correction to nominal values (Gorzkowski et al. 2004)

	Measured (corrected)	Measured (un-corrected)	Nominal
Mg	1.6	1.2	1.7
Nb	12.7	12.8	12.7
Pb	65.4	75.6	65.3
O	15.1	5.5	15.1
Ti	5.2	4.9	5.2
Total	100.0	100.0	100

Table 17.5 compares experimentally determined compositions with the theoretical values of the Pb-based oxide (this is the same specimen as shown in Fig. 17.26). As shown in Fig. 17.28, the quantified oxygen composition is ~1/3 unless we apply the absorption correction to the oxygen Kα. In the ζ-factor method, the X-ray absorption correction is incorporated as we described above and the ζ-factor method has already been shown to work well for several light-element (oxide) quantifications, even for these difficult Pb-based oxides.

Extraction of Thickness-Related Information: Knowing the local composition and thickness via the ζ-factor method allows you to extract further information related to your specimen thickness, such as the beam broadening and the spatial resolution, as described in Sect. 36.1 in W&C. For example, the spatial resolution R can be estimated using the equation proposed by Van Cappellen and Schmitz (1992), derived from the Gaussian beam-broadening model

$$R = q\left[\sigma^2 + \beta(\kappa t)^3/2\right]^{1/2} \tag{17.28}$$

where the scaling parameters q and κ are dependent on the chosen fraction of the incident intensity, *e.g.,* $q = 4.29$ and $\kappa = 0.68$ for the spatial resolution which contains 90% of the incident intensity, which corresponds to the beam diameter at a thickness of $0.68\,t$ from the top surface. The terms σ and β are associated with the incident-beam size and the beam broadening, respectively, and are given by

$$\sigma = d_{TM}/4.29, \quad \beta = 500\left(\frac{4\bar{Z}}{E_0}\right)^2\left(\frac{\rho}{\bar{M}}\right) \tag{17.29}$$

where d_{TM} is the incident beam diameter at full-width-tenth-maximum (FWTM), E_0 is the incident beam energy (in eV), $\bar{Z}$ and $\bar{M}$ are the averaged atomic number and atomic weight, respectively. Since we can determine all the terms related to the specimen by the ζ-factor method, we can easily extract R at individual measured points if d_{TM} and E_0 are known. You should note that the

Gaussian beam-broadening model is the best description of the interaction volume, as was determined by careful evaluation of experimental and simulated concentration profiles. Figure 17.29 shows a set of maps of impurity segregation in a low-alloy steel. Map (a) is an ADF-STEM image in a vicinity of a grain boundary. Composition maps of (b) Ni and (c) Mo were determined by the ζ-factor method (this particular set of maps is also shown in Fig. 35.11 in W&C), together with (d) thickness and (g) R maps. The R map was determined using Eq. 17.28 and shows that the R value around the GB is ~4 nm, which is consistent with the experimentally determined spatial resolution from the concentration profiles across the GB.

The knowledge of local compositions and thickness determined by the ζ-factor method allows us to deconvolute any thickness contribution (i.e., the beam broadening) from the compositions we measure. You'll find that such deconvolution of the thickness contribution can be essential for quantification of fine features embedded in a matrix or on support materials. For example, in quantifying impurity segregation levels at an interface or a grain boundary, the impurity composition you determine may vary depending on the incident probe size, the specimen thickness, the accelerating voltage, *etc*. The boundary enrichment of impurity element A, which is defined as a number of segregant atoms per unit area Γ^{ex}, can be determined as (see Alber et al. 1997).

> **Stating the Obvious – Don't Ignore It**
>
> If your results vary with the experimental conditions, then the composition measurements can't be quantitative. ◄

$$\Gamma_{\mathrm{A}}^{\mathrm{ex}} + \Gamma_{\mathrm{A}}^{\mathrm{bk}} = N_{\mathrm{bk}} \frac{C_{\mathrm{A}}}{C_{\mathrm{B}}} \frac{A_{\mathrm{B}}}{A_{\mathrm{A}}} \frac{V}{A} \tag{17.30}$$

where Γ^{bk} is the number of solute atoms per unit area in the bulk, N_{bk} is the number of atoms per unit volume in the surrounding bulk region, and A_{A} and A_{B} are the atomic weights for A and B. In addition, V and A are the interaction volume and the area of the boundary inside the interaction volume, respectively. Obviously, the major requirement to determine Γ^{ex} is knowledge of V and A, which are dependent on the specimen thickness. Since the diameter of the interaction volume in the Gaussian beam-broadening model is given as $q(\sigma^2 + \beta z^3/2)^{1/2}$ at the depth z from the beam-entrance surface (see Van Cappellen and Schmitz 1992), both V and A can be given as

$$V = \int_0^t \pi \left[q(\sigma^2 + \beta z^3/2)^{1/2}/2 \right]^2 \, \mathrm{d}z = \frac{\pi q^2}{32} (8\sigma^2 t + \beta t^4) \tag{17.31}$$

$$A = \int_0^t \left[q(\sigma^2 + \beta z^3/2)^{1/2} \right] \mathrm{d}z \tag{17.32}$$
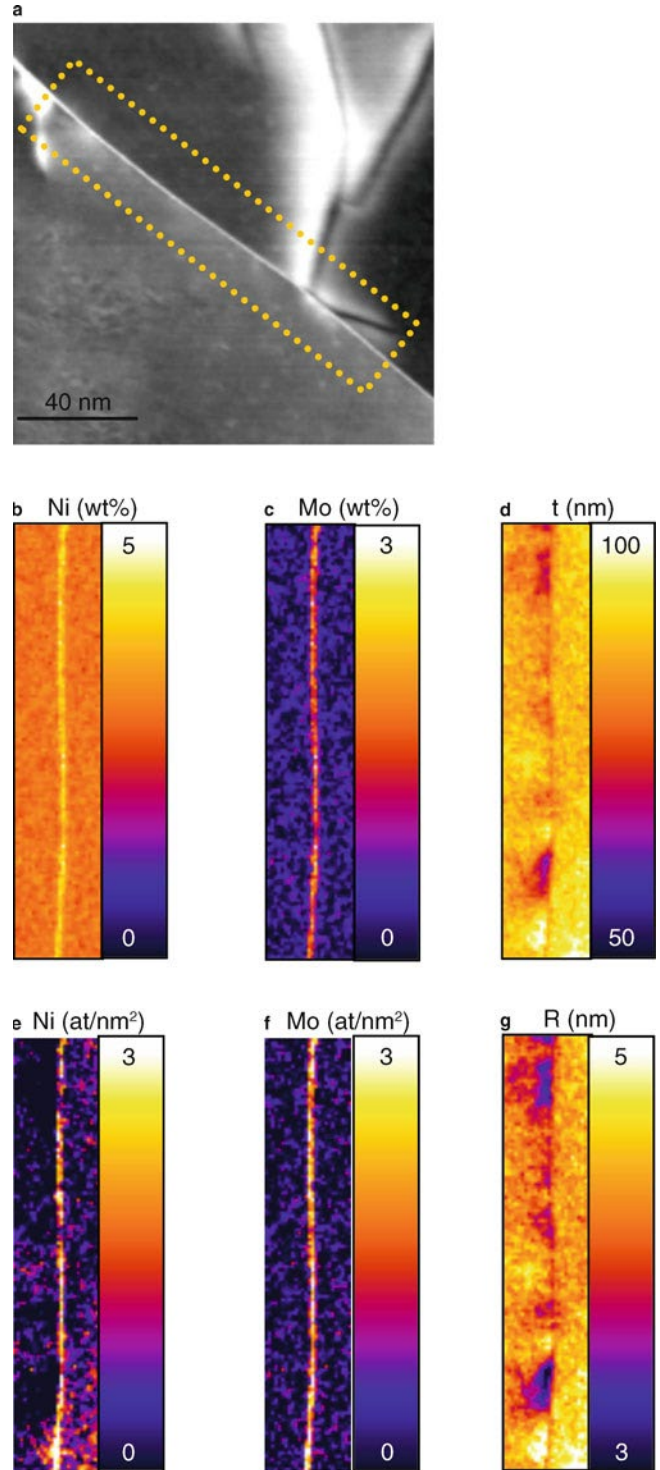
Fig. 17.29 Summary of an application of the ζ-factor method to quantification of boundary segregation in a low-alloy steel. **a** ADF-STEM image in the vicinity of a grain boundary, **b** Ni composition, **c** Mo composition, **d** thickness, **e** Ni boundary excess, **f** Mo boundary excess, and **g** R maps

In Fig. 17.29, maps of the boundary enrichment Γ^{ex} for Ni (e) and Mo (f) determined using Eq. 17.30 are also shown. The average Γ^{ex} values for Ni and Mo determined from the maps are 3.5 ± 0.4 and 4.8 ± 0.1 atoms/nm^2, respectively. Since a single monolayer is ~19 atoms/nm^2 in the closed packed (110) plane for bcc Fe, the enrichments of Ni and Mo can be estimated as less than ~25%. Since the thickness contribution is deconvoluted in the form of the boundary enrichment, the composition can now be transformed to a truly quantitative measure. This thickness deconvolution approach is also applicable when you need to extract the true composition of a precipitate/particle embedded in matrix/support materials.

Evaluation of Analytical Sensitivity: In Sect. 36.2 in W&C, determination of the MMF for the ratio method is summarized. By spectrum simulation in DTSA, we can predict the analytical sensitivity as we just described. The MMF value can also be determined in the ζ-factor method. The criterion for the minimum detectable peak-intensity in an X-ray spectrum is defined as (Romig, Goldstein 1979)

$$I > 3\sqrt{2B} \tag{17.33}$$

where I is the X-ray peak intensity above the background and B is the background intensity. We can incorporate this criterion into the ζ-factor method to describe the MMF

$$\text{MMF}_A = \frac{\zeta_A 3\sqrt{2B_A}}{D_e \rho t} \tag{17.34}$$

In addition to the MMF, the other descriptions of analytical sensitivity, i.e., MDM or MDA can also be derived by the ζ-factor method. As we described in the previous section, information on the analyzed volume is required if you wish to determine the MDA. Since the analyzed volume is given in Eq. 17.31, you can determine the total number of atoms in the analyzed volume as $N_v \rho V/\bar{A}$ (where $\bar{A}$ is the averaged atomic weight). Therefore, you can estimate the MDA for individual elements by multiplying the total number of atoms in the analyzed volume with MMF values in units of atomic fraction.

Determination of Detector Parameters: As with the Cliff–Lorimer k factor, the ζ factor also depends on the X-ray detection efficiency. Since we define the ζ-factor for an individual element, the X-ray collection efficiency (controlled by the detector collection angle in different instruments) can be compared with the ζ-factor values. As shown in Fig. 17.27, the ζ-factor values in the JEOL ARM are ~1/3 of those in the VG HB603. We can interpret this to show that the analytical sensitivity in the ARM is ~ three times higher than that in the HB603. From the reported value of the X-ray collection angle in the HB603, we can estimate the solid angle of the large-angle SDD in the ARM as ~0.53 sr by taking into account the difference in the ionization cross-section at different kV. (note: by further optimization of the SDD position, the solid-angle increases as high as 0.64 sr in the ARM)

Furthermore, as mentioned above, we can determine the thickness values of the detector window materials during the ζ-factor esti-
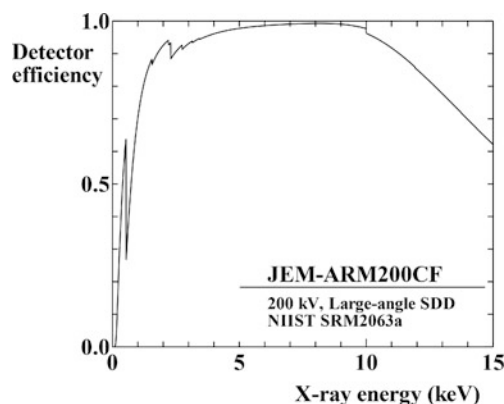

Fig. 17.30 Detector efficiency curve for a JEOL JEM2-ARM200CF with a JEOL Centurio X-ray detector (Watanabe and Wade 2013)

mation. Using the thickness values of the detector window, we can estimate the detector efficiency. Figure 17.30 shows the detector efficiency of the large-angle SDD calculated from the determined thickness values of detector window materials, plotted as a function of the X-ray energy. Note that the decrease of the detector efficiency after ~10 keV is due to the thinner crystal in the SDD.

So in summary, there are several clear advantages to the ζ-factor method over the conventional Cliff–Lorimer ratio method; not only for quantification but also for more detailed analysis of specimens. In addition, you can more easily estimate the XEDS detector parameters and compare the performances of individual instruments as well.

17.4 Contemporary Aplications of X-ray Analysis

In recent years the development of aberration-correction technology in both TEM and STEM has brought a paradigm shift in materials characterization. Just in terms of image resolution, sub-Å resolution is now routinely available (to anyone with enough money) and currently the latest aberration-corrected microscopes offer 0.5 Å resolution both in STEM and TEM modes (Erni et al. 2009; Sawada et al. 2009). Especially in STEM, we now use an incident probe refined by aberration correction to improve the spatial resolution of analysis by both EELS and XEDS.

More importantly, we find that the analytical sensitivity can also be improved because more current can be included in the refined probe while maintaining fine probe dimensions. Since these aberration-correction STEM instruments appeared, X-ray analysis is now seeing a resurgence of interest bolstered by the simple nature and robustness of the quantification procedures which we have just described in great detail.

Both the hardware and software related to X-ray analysis, especially in aberration-corrected STEM, continue to improve. In this
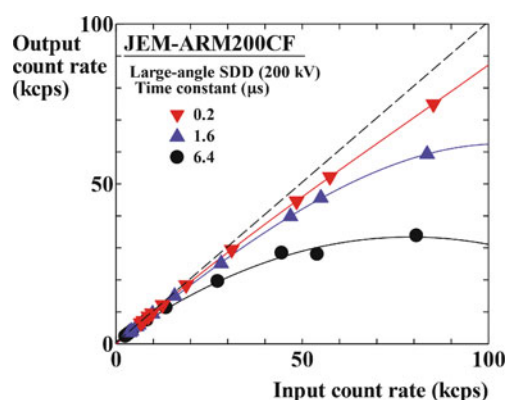
Fig. 17.31 Comparison of input/output count rate of a large solid-angle SDD at three different time constants on an aberration-corrected STEM JEM-ARM200CF

section, we'll introduce you to the latest instrumentation related to X-ray analysis in STEM. Then, we'll give you two examples of more recent applications of X-ray analysis.

17.4.1 Renaissance of X-ray Analysis

Aberration-corrected STEM instruments have triggered further interest in X-ray analysis as we just above. However, in comparison to EELS, the collectable fraction of the generated X-ray signals remains extremely limited (at most ~a few percent). This miserable collection efficiency is still the major limitation of X-ray analysis, even in the aberration-corrected instruments. To some extent we can mitigate this drawback by using a silicon drift detector (SDD). The latest SDD technologies are relatively flexible and so we can fabricate more complex detector arrangements. Several new detector geometries have been proposed. For example, an annular detector geometry (similar to a BSE detector in SEM) has been proposed by Kotula et al. (2009). Zaluzec (2009) has proposed a post-specimen geometry for X-ray collection in the forward-scattering direction of electrons, which allows the collection angle of π sr out of the 4π sr sphere (more than 10 times higher than the conventional detector geometry in AEM!).

As we show in Fig. 17.31, the high throughput capability of the SDD can handle high count rates (up to ~100 kcps) taking advantage of the new geometries. Furthermore, if we integrate the new detector configurations into aberration-corrected instruments, e.g., the FEI Chemi/STEM technology and the JEOL large-angle SDD system, we get detector solid-angles up to ~1 sr (3–10 times higher than conventional systems). Figure 17.32 shows two sets of X-ray maps acquired from TiO_2-supported Au nano particles in a JEOL JEM-ARM200F aberration-corrected STEM with the large collection-angle SDD system. The Au map and color overlay map (*B*) were acquired for 1 min in total. While these maps are still noisy, obtaining such X-ray maps with such very short acquisition times is an amazing advance over prior
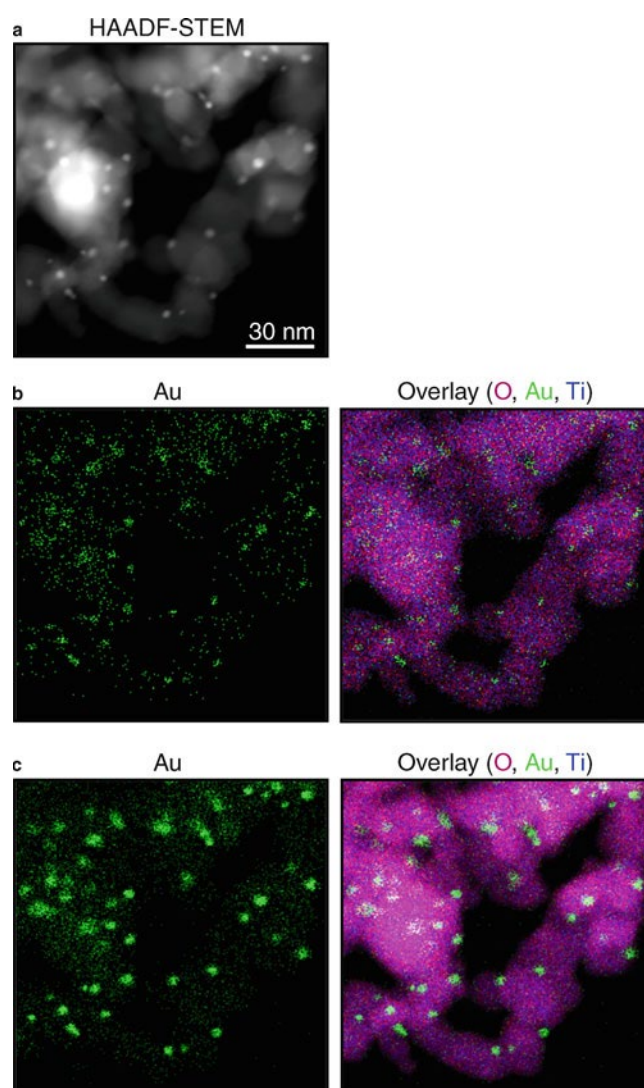
Fig. 17.32 a HAADF-STEM image of TiO_2-supported Au nanoparticles and X-ray maps of Au (*left*) and RGB color overlay with O, Au and Ti (*right*), acquired using an JEOL JEM-ARM200F with the large collection angle SDD system: total acquisition times are (**b**) 1 min and (**c**) 6 min

technologies. If we acquire these maps for a bit longer (still only 6 min!) we can easily see the distribution of Au nano particles in Fig. 17.32c. In the following sections, we summarize two novel applications of X-ray analysis, which again can only benefit from aberration correction and SDD technology.
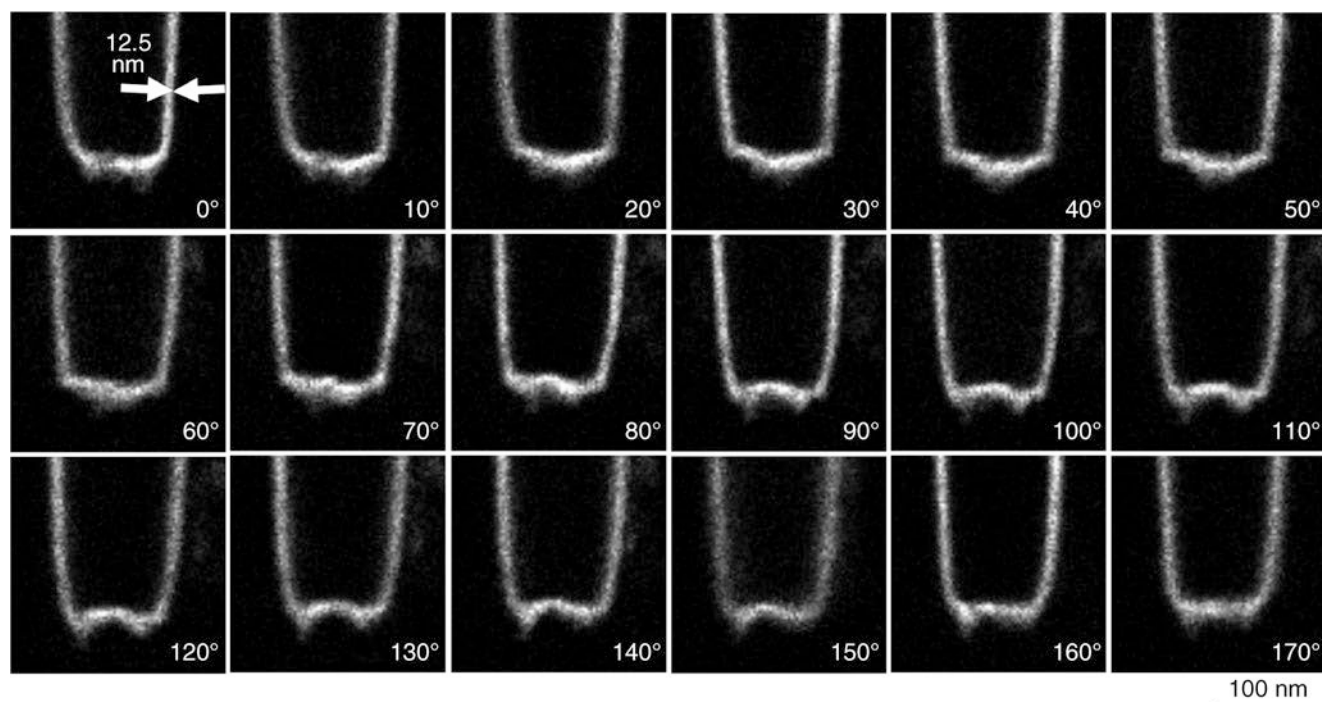
Fig. 17.33 Tilt series of Ti Kα maps around a W contact-plug in a pillar-shaped specimen at different tilt angles between 0° and 170° with 10° steps. Signals in these elemental maps were enhanced by applying the MSA reconstruction to the original X-ray SIs

> **Beginning – A Big Change**
>
> We can maximize the X-ray collection efficiency by using arrays of SDDs (FEI, Harrach et al. 2009) by using an SDD with a very large active area (JEOL, Ohnishi et al. 2011) ◀

17.4.2 XEDS Tomography for 3D Elemental Distribution

In TEM, we usually view the projected image of a thin specimen, which means that information in the optic-axis direction (the z direction) is not obtainable unless we tilt the specimen. If we want to observe the microstructure through the depth of the specimen, we have to use either stereo microscopy (see Sect. 29.1 in W&C) or electron tomography (introduced for EELS in Sect. 40.9 in W&C). This latter approach requires that multiple images be recorded at various tilt angles to give you the most accurate 3D reconstruction. Much more information can be found in Chap. 12 on electron tomography.

Although you can image the 3D microstructure by electron tomography, it would be still be difficult to infer elemental distributions in the z direction through your specimen. Fortunately both EELS and XEDS can give you 3D elemental distributions. However, XEDS-based tomography has seen little usage because of the poor efficiencies of X-ray generation and detection (again!). In addition, if you use a conventional TEM holder for tomographic XEDS analysis, the path length of the X-rays and hence the X-ray absorption change as you change the tilting angle (Möbus et al. 2003). Once again, at larger tilt angles, X-ray absorption in your specimen becomes the limiting factor.

We can solve the problem of differences in X-ray absorption at different tilt angles by using a pillar-shape specimen with a specially designed specimen holder. Figure 17.33 shows a tilt series of Ti Kα maps acquired from a pillar-shaped Si device around a W contact plug, using a Hitachi HD-2300 dedicated STEM. The tilt-series of X-ray SIs were acquired over a tilt range from 0 to 175° with five steps. To compensate for the weak X-ray signals, multivariate statistical analysis (MSA) was applied. (See Chap. 16 for much more on MSA.) The Ti distributions show the metallization layer around the W plug. You can see this layer more clearly in the reconstructed Ti distribution shown in Fig. 17.34. The complex Ti distribution, especially at the bottom part of the pillar, is barely observable in a single X-ray map. So in a conventional XEDS configuration, weak signal enhancement, e.g., by MSA, is essential if you want to see an XEDS tomographic image. Not surprisingly, XEDS tomography is much more suited to an aberration-corrected STEM with an SDD X-ray system.
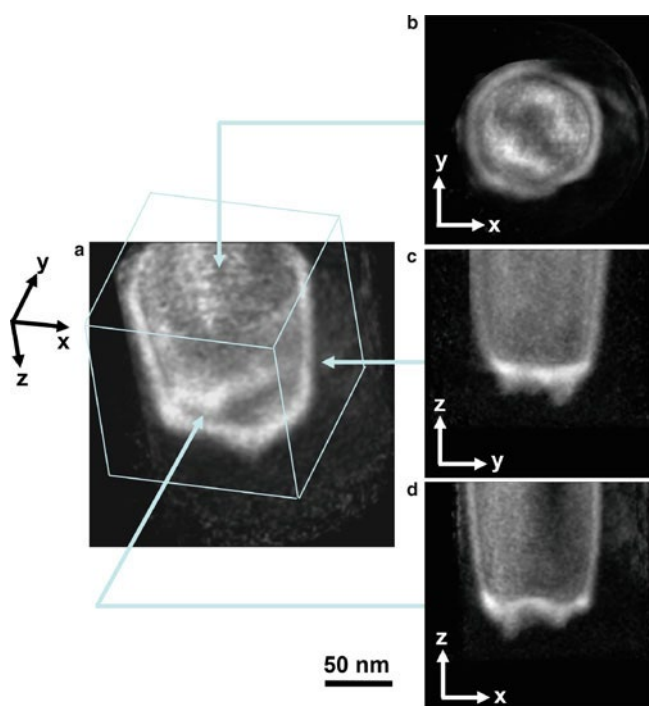
Fig. 17.34 a 3D-reconstructed Ti distribution around the W contact-plug created using 37 Ti K maps at tilt angles between 0°–180° with a 5° step, partially shown in Fig. 17.33: **a** at 45° from all primary *x, y* and *z* axes and 2D projected Ti distributions along the *z* axis (**b**), *x* axis (**c**), and *y* axis (**d**)

Figure 17.35 shows another example of XEDS tomography from an In-doped GaN nano pyramid structure for light emitting diode applications. In Fig. 17.35a, HAADF-STEM image and a set of elemental maps of Ga, N and In are shown, which were obtained using an instrument with an SDD X-ray collection system. You can see that the In dopant is mainly located at the top of the pyramid structure. In this field of view, the XEDS tomographic series was acquired by recording two orthogonal-axis tilt-series of X-ray spectrum images with ±60° in 3° steps (in total, 80 XEDS spectrum images). This took a total acquisition time of ~8 h. If you use an instrument with improved X-ray collection efficiency, you can now acquire dual-axis XEDS tomography series in such reasonable times. Selected slices of the In distribution reconstructed from the dual-axes XEDS tomography datasets are shown in Fig. 17.35b. You can see that In is located not only at the top of the nano pyramid structure but also along the sides of the pyramid. Again, this information is not obtainable from a single 2D-projected image or X-ray map.

17.4.3 Atomic Resolution X-ray Mapping

If you have access to an aberration-corrected STEM, atomic resolution EELS mapping can be routine. Conversely, such

atomic resolution is still a challenge for X-ray analysis because of its inherently poorer signal collection efficiency (~100 times worse than EELS). Therefore, if we want to approach atomic-level resolution X-ray analysis, either we need much greater beam currents (which may induce radiation damage and degrade spatial resolution) or we need to collect our signals for much longer acquisition time (which means more spatial drift). Fortunately, in the best instruments today, the mechanical and electrical stabilities have been significantly improved and large-angle SDDs are routine. In fact, as shown in Fig. 35.11 in W&C, the spatial resolution of X-ray analysis (in 2009) was ~0.4 nm. Additionally, as you can now see in Fig. 17.24b, DTSA simulation suggests that the analytical sensitivity in terms of MDA may already have reached the single-atom level in an aberration-corrected STEM.

Figure 17.36 shows a set of X-ray maps with (a) a HAADF-STEM image from interfaces in a [100]-projected $LaMnO_3$/$SrTiO_3$ multilayer thin-film, acquired by using the JEM-ARM200CF with a large collection-angle XEDS detector. The X-ray maps were acquired in the SI mode with 256×256 pixels for a frame time of 50 ms. The total acquisition time was ~40 min and spatial-drift correction was applied during acquisition. The bright and slightly fainter spots appearing in the HAADF-STEM image correspond to heavy atomic columns of La or Sr and to Ti-O or Mn-O columns in the perovskite structure, respectively. From the extracted elemental maps, two RGB color-overlay images were constructed, as you can see in Fig. 17.36 (g, Red: La L, Green: Mn K and Blue: O K) and (h, Red: Sr L, Green: Ti K and Blue: O K), which represent $LaMnO_3$ and $SrTiO_3$ layers, respectively. So we can obtain elemental distributions from much larger fields of view, if we take advantage of the improved stability in the latest instruments, such as the JEM-ARM200CF.

An atomic-resolution X-ray SI data set was acquired from a [100]-projected GaAs specimen using the aberration-corrected STEM JEM-ARM200CF. Once we obtain such atomic resolution elemental maps in the latest instruments, can we quantify them? To see how well we can do this, the maps were analyzed by the ζ-factor method. Figure 17.37 shows a set of ζ-factor-processed elemental and compositional X-ray maps along with an HAADF-STEM image. In the [100]-projection of GaAs, Ga and As layers are alternatively separated. As shown in the elemental maps of Ga and As with their color overlay, atomic layers of Ga and As are separated as expected. Conversely in the quantified compositional maps, the compositions do not reach the expected 0 at% or 100 at% in the corresponding atomic layers. The average compositions of whole Ga and As maps were calculated to be 50.8 and 49.2 at%, respectively, which are very close to the nominal value (50:50). Thus, the quantification itself was performed correctly.

So why do we not see the correct values for the individual atomic columns? The deviations in compositions from the expected values (0 or 100 at%) are partially due to the beam broadening. According to the thickness map (Fig. 17.37), there appear to be relatively large thickness variations between on-column and

Chapter 17
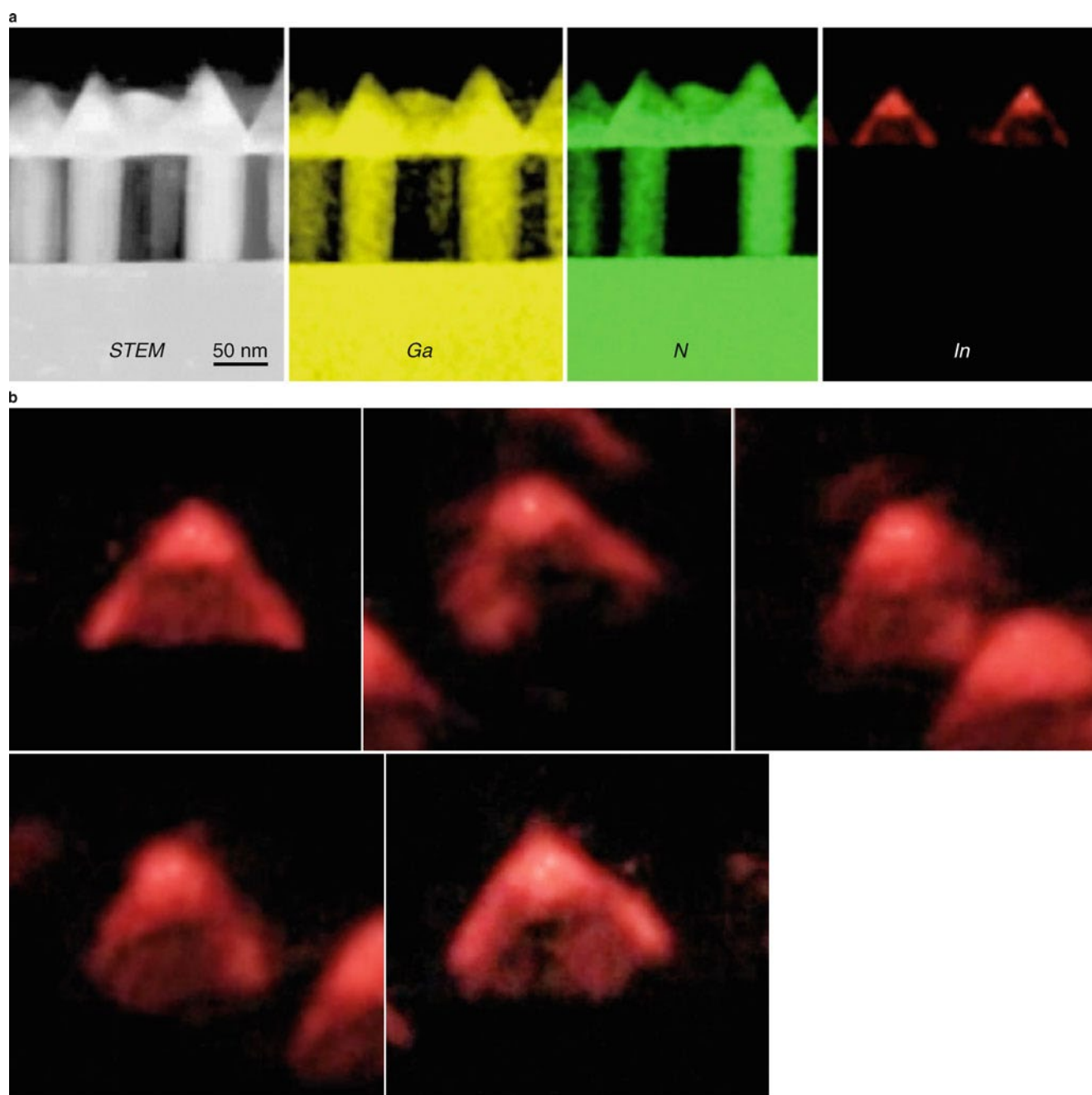
Fig. 17.35 a HAADF-STEM image and a set of elemental maps of Ga, N, and In obtained from an In doped GaN nano pyramid structure using an instrument with an improved X-ray collection system. **b** Selected slices of the In distribution around one of the pyramid structures reconstructed from the dual-axes XEDS tomography datasets (two orthogonal-axis tilt-series of X-ray spectrum images with ± 60° in 3° steps)
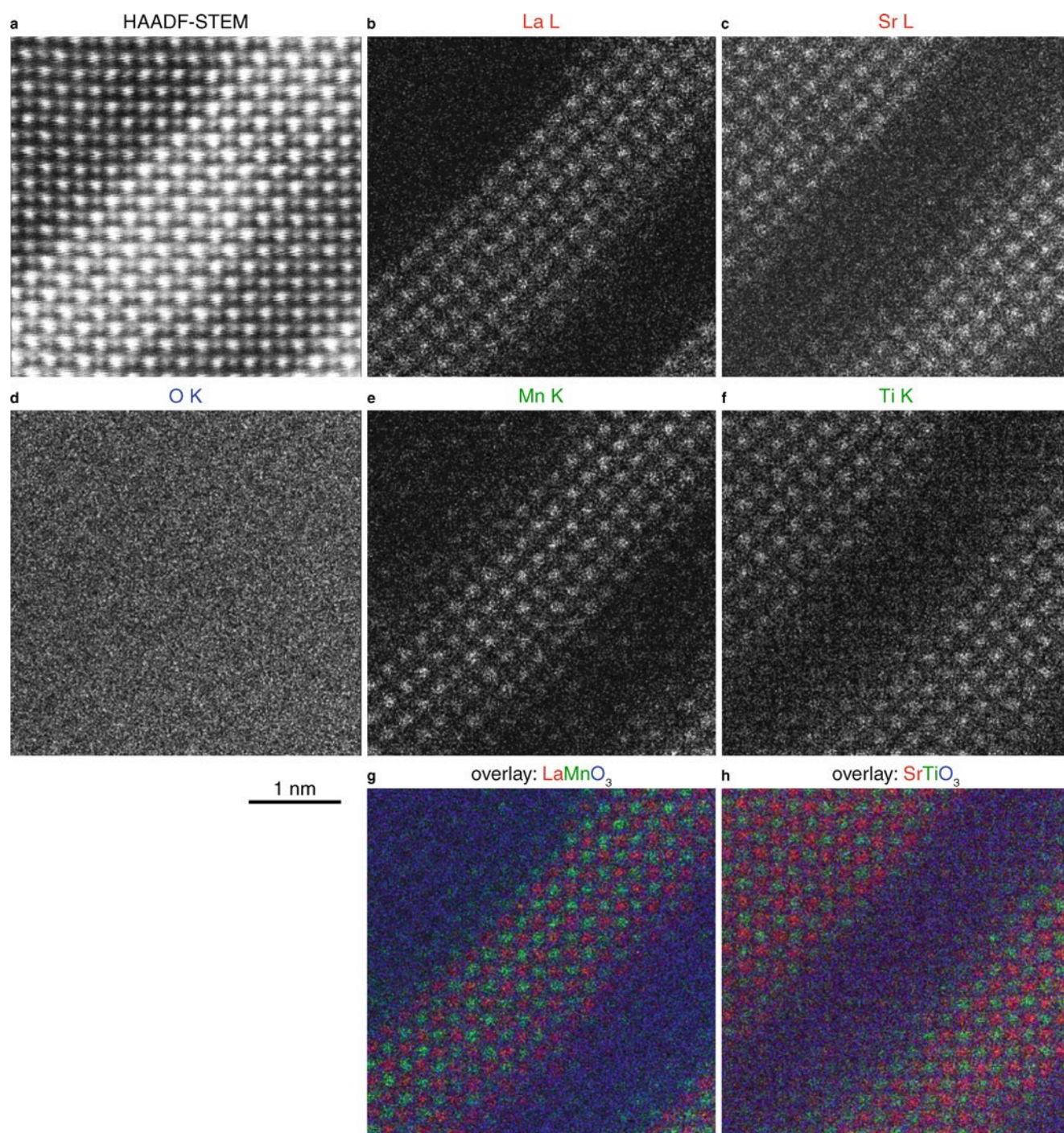
Fig. 17.36 a An HAADF-STEM image from a $LaMnO_3/SrTiO_3$ interface, elemental maps of (**b**) La, (**c**) Sr, (**d**) O, (**e**) Mn, (**f**) Ti, (**g**) RGB color-overlay image of $LaMnO_3$ and RGB color-overlay image of $SrTiO_3$
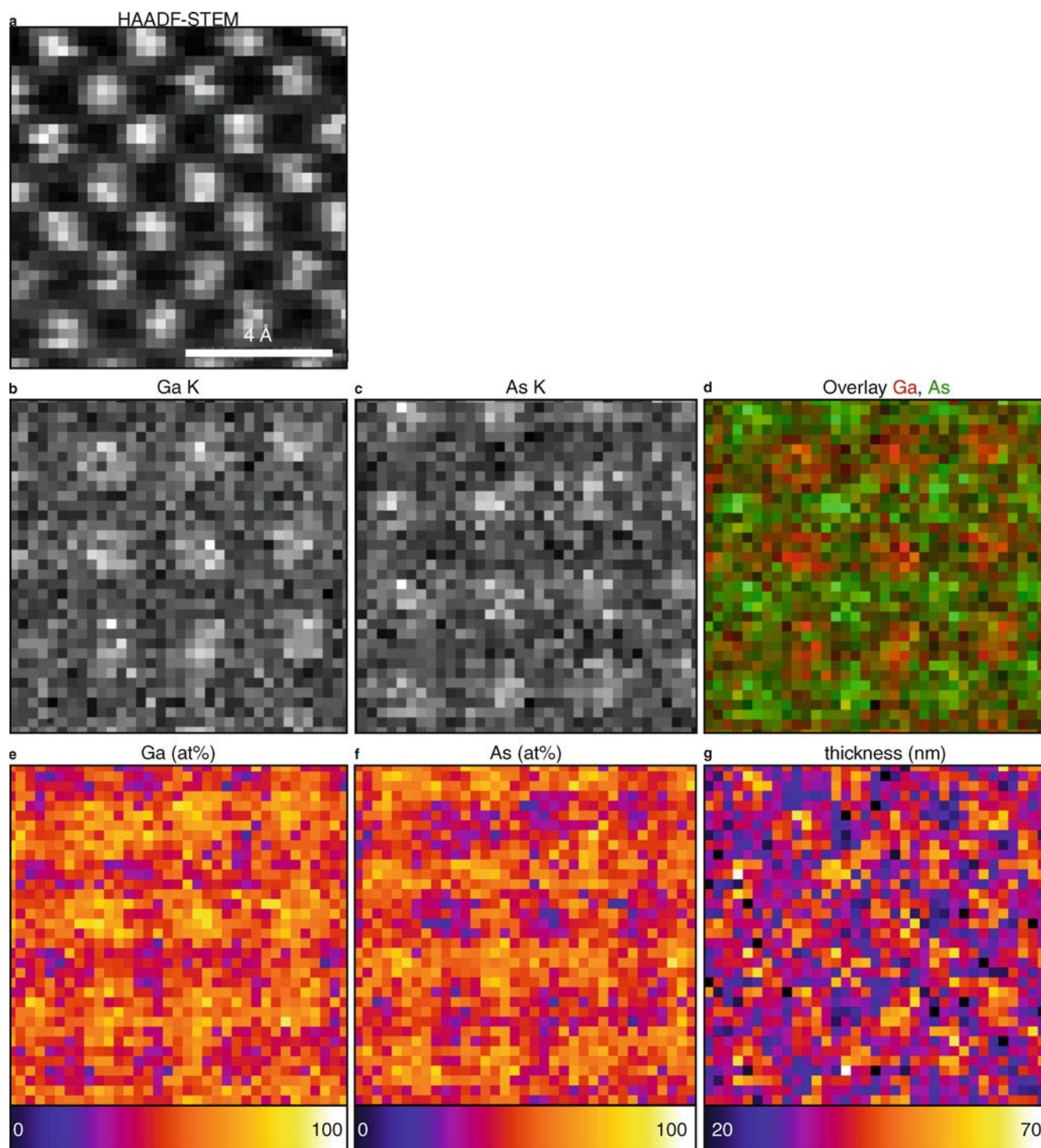
Fig. 17.37 Set of quantitative X-ray maps from a [100]-projected GaAs specimen: **a** HAADF-STEM image, **b** Ga K intensity, **c** As K intensity, **d** color overlay of Ga K (*red*) and As K (*green*), **e** Ga composition, **f** As composition, and **g** thickness

off-column regions: ~60 nm and 30 nm at on- and off-column regions, respectively. It is most unlikely that local specimen thickness changes of this magnitude would occur from column to column. Because the specimen thickness was determined directly from the X-ray intensities of Ga K and As K lines, such thickness enhancement at the on-column regions indicates that abnormal X-ray emission occurs due to channeling. Because the map was obtained in a highly symmetric zone axis orientation, we might expect the incident beam propagation to be influenced by the atomic arrangement, i.e., the incident electrons are channeled and de-channeled.

In AEM

Always keep in mind beam broadening and channeling.

◄

When de-channeling of the incident electrons occurs, they generate X-ray signals from neighboring columns. So, we can conclude that, in addition to regular beam broadening de-channeling is another reason for the apparent deviations in compositions from the expected single column values. When we are quantifying such atomic resolution X-ray maps, we might not need to include the correction for X-ray absorption because the specimens are thin enough for atomic resolution imaging and analysis. Instead, we now have to consider the channeling correction in quantitative X-ray analyses at the atomic level, which is why you've already read about channeling in several previous chapters.

Chapter Summary

In this chapter, we reviewed four independent subjects related to the X-ray analysis of thin specimens in TEM to augment the contents of Chaps. 32–36 in W&C.

In the first section, we summarized the systematic procedures to characterize XEDS spectrometers attached to TEMs. You can determine several fundamental parameters such as the energy resolution (as a function of the process time), IHC, *P/B*, etc., from a single spectrum of a standard NiOx thin specimen. We recommend that these parameters be characterized at least once (preferably prior to first operating the microscope). In addition, you should also monitor the detector performance by periodically measuring spectra from the NiOx.

The second section comprises a comprehensive tutorial of X-ray simulation through the NIST DTSA software package. Then, we described the fundamental physics related to X-ray generation and detection through simulated X-ray spectra, which are never seen in practice. From these simulated spectra, you can learn detailed aspects of X-ray spectrometry. Additionally, we went through four applications of X-ray spectrum simulation including the estimation of X-ray absorption and calculation of analytical sensitivity. If

you use DTSA to first simulate the X-ray spectra from your experimental specimen prior to actual analyzing them, you would save time (and perhaps money).

In W&C, several procedures for quantitative X-ray analysis are summarized, including a brief introduction to the ζ-factor method. So in the third section, we went into much greater detail concerning this quantitative analysis method. In addition, we compared the ζ-factor method with the conventional Cliff–Lorimer *k*-factor approach and showed that the ζ-factor was much better if the specimen was thick, if absorption was a problem (which it is for light element X-rays) and if k-factor standards were difficult to obtain (which they usually are!).

In the last section of this chapter, we introduced several contemporary applications of X-ray analysis. Because of the recent availabilities of aberration-correction columns in combination with the latest developments of SDD technology, the popularity of X-ray analysis has been revived. With such instrumentation X-ray analysis can now be used to obtain 3D elemental distributions and atomic-resolution elemental distributions. When W&C was first penned, such advanced applications were merely a dream. Now they are a reality!

Chapter 17

Appendix

People

Chuck Fiori (1938–September 15, 1992). The DeskTop Spectrum Analyzer (DTSA) software package was originally developed by the late Chuck Fiori with Bob Myklebust and Carol Swyt. They worked at the National Institutes of Standards and Technology (NIST) and the National Institutes of Health (NIH) in late 1980s.

Joseph (Joe) I. Goldstein was born in Syracuse, NY, on January 6, 1939 and died on June 27, 2015; he founded the Lehigh short course, inspired a generation using AEM, and recruited a young DBW to join him.

Questions

Q17.1   Compare and contrast the *k*-factor and the *ζ*-factor approaches to quantification.
Q17.2   What is the single most important variable that affects your decision to use either of these two approaches? Explain why you chose that variable.
Q17.3   Why should you simulate the spectra that you hope will be generated from your specimen before proceeding to gather them experimentally?
Q17.4   What can you do to minimize ice and carbon contamination on your XEDS detector
Q17.5   Why has it proven so difficult to detect single atoms in thin foils using XEDS while EELS has been able to do this for many years?
Q17.6   Distinguish the several different definitions we use for analytical sensitivity.
Q17.7   Why does a single column of atoms in a thin foil not give rise to an XEDS spectrum containing the signal from these atoms alone?
Q17.8   What does your answer to question 17.5 lead you to conclude about the real spatial resolution of analysis by XEDS?
Q17.9   Why are there so many characteristics of your XEDS detector that you have to determine prior to XEDS analysis when, by comparison, an EEL spectrometer is relatively free of such requirements?
Q17.10   If you have a single atom of element B in an analyzed volume containing 100 atoms of element A, can you estimate, to a first approximation, how long you need to gather a spectrum in order to say with 99% confidence that that atom of A is present. Choose a reasonable set of experimental variables (including kV, beam current

probe size, detector collection angle etc.). State any further assumptions.
Q17.11   Simulate X-ray spectra to confirm the conditions (the beam current, specimen thickness, acquisition time and accelerating voltage) for 1.0 wt% and 0.3 wt% detection levels of a high Z element in a relatively low *Z* material, e.g., Cu in Al.
Q17.12   Similar to the above question; simulate X-ray spectra to confirm the conditions for 1.0 wt% and 0.3 wt% detection levels of a low Z element in a relatively high Z material, e.g., P in Ga.
Q17.13   Questions 17.11 and 17.12 are for estimation of minimum mass fraction (MMF). Based on your estimated conditions in the above question, how many solute atoms are included. The number of solute atoms is equivalent to the minimum detectable mass (MDM).
Q17.14   Plot the absorption loss curves of major X-ray lines in your materials systems using Eq. 17.27 and estimate the critical specimen thickness below 10% absorption.
Q17.15   Using Eq. 17.28, estimate spatial resolution values for your specimen in conventional and aberration-corrected AEMs, and plotted as a function of the specimen thickness. This plot is essentially same as Fig. 36.5c in W&C. Using this plot, determine the required specimen thickness especially for the aberration-corrected AEM.

Appendix 1. Error Analysis in the *ζ*-factor Method

As described in Sect. 17.3.3, we need an iterative calculation for determination of compositions and specimen thickness including the absorption correction in the *ζ*-factor method. It is not very straightforward to estimate errors in such an iterative process but there is an alternative approach for the error calculation. In an *n* component system, we determine compositions and thickness from *n* characteristic X-ray intensities via *n* *ζ* factors in the *ζ*-factor method. Obviously, both the *n* X-ray intensities and *n* *ζ* factors are independent variables, and their errors need to be taken into account if you want to determine the error estimation independently. Let's denote the errors in X-ray intensity and the *ζ* factor for the *j*th component as ΔI_j and $\Delta \zeta_j$, respectively.

First, we determine the error-free composition(s) C_i and thickness *t* from *n* intensities and *n* *ζ* factors without their errors. Then, we calculate the compositions and thickness with an error contribution of *j*th X-ray intensity by substituting $I_j + \Delta I_j$ for I_j. The composition and thickness with the error of *j*th intensity are expressed as $C_i(\Delta I_j)$ and $t(\Delta I_j)$, respectively. You have to repeat

this process for all X-ray intensities independently. Similarly, the errors in each individual ζ-factor are incorporated by substituting $\zeta_j + \Delta\zeta_j$ for ζ_j, and composition and thickness with errors of the z-factor are expressed as $C_i(\Delta\zeta_j)$ and $t(\Delta\zeta_j)$, respectively. Finally, the errors in the compositions and thickness are given as:

$$\Delta C_i = \sqrt{\sum_{j=1}^{n} \left[C_i(\Delta\zeta_j) - C_i \right]^2 + \sum_{j=1}^{n} \left[C_i(\Delta I_j) - C_i \right]^2}$$

$$\Delta t = \sqrt{\sum_{j=1}^{n} \left[t(\Delta\zeta_j) - t \right]^2 + \sum_{j=1}^{n} \left[t(\Delta I_j) - t \right]^2}$$

(17.35)

This approach requires $2n$ times extra calculations of compositions and thickness after determination of the error-free values (yes, it is a bit complicated and tedious!). However, we can easily adapt this approach to computational codes and it is applicable to any iterative calculation (e.g., the matrix correction procedures for bulk-sample analysis in an EPMA such as ZAF and $\phi(\rho z)$). The full error analysis procedures for the ζ-factor determination and estimation can be found in the paper by Watanabe and Williams (2006).

Appendix 2. Calculation of the Specimen Density

In the ζ-factor method, we first determine the specimen thickness as the mass thickness ρt as we described above. To convert the mass thickness to the absolute specimen thickness, we need values of the specimen density at individual analysis points. The specimen density can be estimated from Eq. 35.27 in W&C, i.e., the mass divided by the unit-cell volume. So we need some crystallographic information to determine the unit-cell volume. Otherwise, the density can be calculated as a first approximation by taking a weighted mean ($\rho = \Sigma C_j \rho_j$) or a harmonic mean ($1/\rho = \Sigma C_j/\rho_j$) from the density values of the individual component elements.

For example, Fig. 17.38 shows the composition dependence of the specimen density in the Au-Cu system. All the symbols in this figure represent the densities calculated from reported lattice parameters using Eq. 35.27 in W&C. The dashed and solid lines indicate the estimated values from the simple weighted mean and the harmonic mean, respectively. The ρ values estimated by the harmonic mean describe the density very well. In fact, the harmonic-mean approach may work especially well for close-packed condensed systems, such as metallic alloys and intermetallic compounds. For other materials systems such as ceramics and glasses (even not crystalline), the density value needs to be estimated differently.
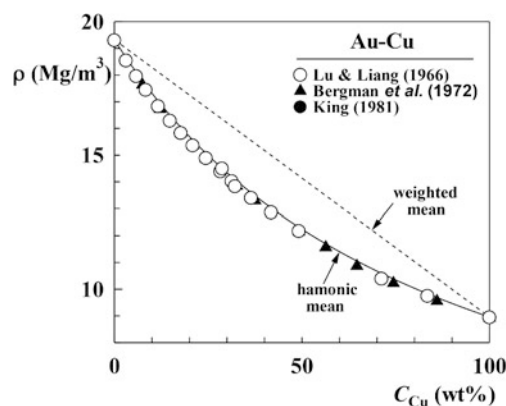

Fig. 17.38 Comparison of calculated density values by weighted (*dashed line*) and harmonic (*solid line*) means with those determined from reported lattice parameters summarized by Okamoto et al (1987)

References

General References

Lyman CE, Newbury DE, Goldstein JI, Williams DB, Romig AD Jr., Armstrong JT, Echlin PE, Fiori CE, Joy D, Lifshin E, Peters KR (1990) Scanning Electron Microscopy, X-Ray Microanalysis and Analytical Electron Microscopy; A Laboratory Workbook. Plenum Press, New York

Williams DB, Goldstein JI (1991) Quantitative X-ray Microanalysis in the Analytical Electron Microscope. In: Heinrich KFJ, Newbury DE (eds) Electron Probe Quantification. Plenum Press, New York., pp 371–398

Zemyan SM, Williams DB (1995) Characterizing an Energy-Dispersive Spectrometer on an Analytical Electron Microscope. In: Williams DB, Goldstein JI, Newbury DE (eds) X-Ray Spectrometry in Electron Beam Instruments. Plenum Press, New York., pp 203–219

Specific References

Alber U, Müllejans H, Rühle M (1997) Improved Quantification of Grain Boundary Segregation by EDS. Ultramicroscopy 69:105–116

Bennett JC, Egerton RF (1995) NiO test specimen for analytical electron microscopy: round-robin results. J Microsc Soc Am 1:143–149 (Following up on using NiOx in the journal now known as Microscopy & Microanalysis)

Van Cappellan E, Schmitz A (1992) A Simple Spot-size Versus Pixel-size Criterion for X-ray Microanalysis of Thin Foils. Ultramicroscopy 41:193–199

Cliff G, Lorimer GW (1975) The Quantitative Analysis of Thin Specimens. J Microsc 103:203–207 (Historical classic)

Chapter 17

Egerton RF, Cheng SC (1994) The use of NiO test specimens in analytical electron microscopy. Ultramicroscopy 55:43–54 (All about using NiOx)

Lovejoy TC, Ramasse QM, Falke M, Kaeppel A, Terborg R, Zan R, Dellby N, Krivanek O (2012) Single atom identification by energy dispersive X -ray spectroscopy. Appl Phys Lett 100:154101-1-4

Newbury DE, Ritchie NWM (2015) Performing elemental microanalysis with high accuracy and high precision by scanning electron microscopy/silicon drift detector energy-dispersive X-ray spectrometry (SEM/SDD-EDS. J Mater Sci 50(2):493–518 (A very useful review)

Rose A (1970) Quantum limitations to vision at low light levels. Image Technol 12:13–15 (See also pp. 30–31)

Watanabe M, Williams DB (1999) Atomic-Level Detection by X-ray Microanalysis in the Analytical Electron Microscope. Ultramicroscopy 78:89–101

Watanabe M, Williams DB (2003) Quantification of Elemental Segregation to Lath and Grain Boundaries in Low-alloy Steel by STEM X -ray Mapping Combined with the ζ-factor Method. Z Metallk 94:307–316 (We think that this and the 2006 paper are worth reading!)

Watanabe M, Williams DB (2006) The Quantitative Analysis of Thin Specimens: a Review of Progress from the Cliff-Lorimer to the New ζ-Factor Methods. J Microsc 221:89–109 (As in the 2003 paper, you'll find more details and references to the original work.)

We include more references than usual because this is such a new field. We'll add other references to the website.

References for Software

(http://www.cstl.nist.gov/div837/837.02/epq/dtsa2/index.html).

Brundle D, Uritsky Y, Chernoff D (1996) Real-time simulation for X-ray microanalysis. Solid State Technology 39(3):105–111 (Electron Flight Simulator is commercialized at http://www.small-world.net/efs.htm)

Find a standardized description of the EMSA format through the International Organization for Standardization (ISO 22029:2003). ISO 22029-2003 2003 is the *Standard file format for spectral data exchange.* Also available at ANSI (American National Standard Institute) web site (www.ansi.org).

Find SheepShaver at http://sheepshaver.cebix.net/

Fiori CE, Swyt CR, Myklebust RL (1992) *NIST/NIH Desk Top Spectrum Analyzer.* Public domain software available from the National Institute of Standards and Technology, Gaithersburg, MD. http://www.cstl.nist.gov/div837/Division/outputs/DTSA/DTSA.htm

Ritchie NWM (2008) DTSA-II. Public domain software available from the National Institute of Standards and Technology, Gaithersburg, MD

Watanabe has developed a simple software package as a set of plug-ins for Gatan DigitalMicrograph. This plug-in package is freely available through his home page (http://www.lehigh.edu/~maw3/msh/xutilmain.html). You can find the installa-

tion procedure and usage details in the help file, which comes with the plugin package.

Watanabe has summarized how to install DTSA in Windows on his web site (http://www.lehigh.edu/~maw3/msh/dtsaonwintop.html).

17.1 – XEDS Detector Characterization

Fiori CE, Swyt CR, Ellis JR (1982) The Theoretical Characteristic to Continuum Ratio in Energy Dispersive Analysis in the Analytical Electron Microscope. In: Microbeam Analysis-1982. Ed. Heinrich KFJ, San Francisco Press, San Francisco, CA., pp 57–71

Heinrich KFJ (1987) Mass absorption coefficients for electron probe microanalysis. In: Brown JD, Packwod RH (eds) Proc 11th Int Cong on X-Ray Optics Microanalysis. University of Western Ontario, London., pp 67–377

Hovington P, L'Espérance G, Baril E, Rigaud M (1993) A standard procedure for the modeling of the decrease in detection efficiency with time for low-energy EDS spectra. Microsc Microanal 2:277–288

17.2 – X-ray Spectrum Simulation (see also References for Software above)

Fiori CE, Swyt CR (1989) The use of theoretically generated spectra to estimate detectability limits and concentration variance in energy-dispersive X-ray microanalysis. In: Russell PE (ed) Microbeam Analysis-1989. San Francisco Press, San Francisco, CA.

Newbury DE, Myklebust RL, Swyt CR (1995) The use of simulated standards in quantitative electron probe microanalysis with energy-dispersive X-ray spectrometry. Microbeam Analysis 4:221–238

17.3 – ζ-factor Method

Armigliato A (1992) X-ray Microanalysis in the Analytical Electron Microscope. In: Merli PG, Antisari MV (eds) Electron Microscopy in Materials Science. World Scientific, Singapore, pp 431–456

Gorzkowski EP, Watanabe M, Scotch AM, Chan HM, Harmer MP (2004) Direct Measurement of Oxygen in Lead-Based Ceramics Using the ζ-factor Method in an Analytical Electron Microscope. J Mater Sci 39:6735–6741

Lyman CE, Goldstein JI, Williams DB, Ackland DW, von Harrach HS, Nicholls AW, Statham PJ (1994) High Performance X-ray Detection in a New Analytical Electron Microscopy. J Microsc 176:85–98

Romig AD Jr., Goldstein JI (1979) Detectability Limit and Spatial Resolution in STEM X -ray Analysis: Application to Fe-Ni. In: Newbury DE (ed) Microbeam Analysis – 1979. San Francisco Press, San Francisco, CA., pp 124–128 (The

criterion for the minimum detectable peak-intensity in an X-ray spectrum)

Watanabe M, Wade CA (2013) Practical Measurement of X-ray Detection Performance of a Large Solid-Angle Silicon Drift Detector in an Aberration-Corrected STEM. Microsc Microanal 19(Suppl. 2):1264–1265

17.4 – New Detector Configurations

Erni R, Rossel MD, Kisielowski C, Dahmen U (2009) Atomic-Resolution Imaging with a Sub-50-pm Electron Probe. Phys Rev Lett 102:096101 ((4 pages).)

von Harrach HS, Dona P, Freitag B, Soltau H, Niculae A, Rohde M (2009) An Integrated Silicon Drift Detector System for FEI Schottky Field Emission Transmission Electron Microscopes. Microsc Microanal 15(Suppl. 2):208–209 (The FEI approach)

Kotula PG, Michael JR, Rohde M (2009) Results from Two Four-Channel Si-drift Detectors on an SEM: Conventional and Annular Geometries. Microsc Microanal 15(Suppl. 2):116–117

Ohnishi I, Okunishi E, Yamazaki K, Aota N, Miyatake K, Nakanishi M, Ohkura Y, Kondo Y, Yasunaga K, Toh S, Matsumura S (2011) Development of a Large Solid Angle SDD for TEM and its Applications. Microsc Microanal 17(Suppl. 2):Late Breaking 22 (The JEOL approach)

Sawada H, Tanishiro Y, Ohashi N, Tomita T, Hosokawa F, Kaneyama T, Kondo Y, Takayanagi K (2009) STEM Imaging of 47-pm-Separated Atomic Columns by a Spherical Aberration-Corrected Electron Microscope with a 300-kV Cold Field Emission Gun. J Electron Microsc 58:357–361

Watanabe M (2011) Chapter 7: X-ray Energy Dispersive Spectrometry in Scanning Transmission Electron Microscopes. In: Pennycook SJ, Nellist PD (eds) Scanning Transmission Electron Microscopy: Imaging and Analysis. Springer, New York., pp 291–351

Zaluzec NJ (2009) Innovative Instrumentation for Analysis of Nanoparticles: The π Steradian Detector. Microscopy Today 17(4):56–59

17.4 – XEDS Tomography

Möbus G, Doole RC, Inkson BJ (2003) Spectroscopic electron tomography. Ultramicroscopy 96:433–451

Yaguchi T, Konno M, Kamino T, Watanabe M (2008) Observation of Three-dimensional Elemental Distributions of a Si-device Using a 360-degree-tilt FIB and the Cold Field-emission STEM System. Ultramicroscopy 108:1603–1615 (The Hitachi approach)

Zaluzec NJ (2012) The Confluence of Aberration Correction, Spectroscopy and Multi-Dimensional Data Acquisition. Proc. European Microscopy Congress

17.4 – Atomic Resolution X-ray Analysis

Watanabe M (2013) Microscopy Hacks: Development of Various Techniques to Assist Quantitative Nanoanalysis and Advanced Electron Microscopy. Microscopy 62(2):217–241

17. Appendix 2 – Calculation of Specimen Density

Okamoto H, Chakrabarti DJ, Laughlin DE, Massalski T (1987) The Au-Cu (Gold-Copper) System. Bull Alloy Phase Diagrams 8:454–473

Chapter 17